SELF-ORGANIZED NETWORK OF SILICON OXIDE ON EPITAXIAL GRAPHENE

A Thesis Submitted to
Graduate School of Engineering and Sciences of
İzmir Institute of Technology
in Partial Fulfillment of the Requirements for the Degree of

MASTER OF SCIENCE

in Materials Science and Engineering

by
Dilce ÖZKENDİR

May 2017
İZMİR

We approve the thesis of **Dilce ÖZKENDİR**

Examining Committee Members:

Assoc. Prof. Dr. Cem ÇELEBİ
Department of Physics, İzmir Institute of Technology

Assist. Prof. Dr. Gökhan UTLU
Department of Physics, Ege University

Assist. Prof. Dr. Mehmet Z. BAYKARA
Department of Mechanical Engineering, Bilkent University

31 May 2017

Assoc. Prof. Dr. Cem ÇELEBİ

Supervisor, Department of Physics,
İzmir Institute of Technology

Assist. Prof. Dr. Umut ADEM

Co-Supervisor, Department of Material Science and Engineering
İzmir Institute of Technology

Prof. Dr. Mustafa Muammer DEMİR

Head of the Department of Materials Science and Engineering

Prof. Dr. Aysun SOFUOĞLU

Dean of the Graduate School of Engineering and Sciences

ACKNOWLEDGEMENTS

It is my pleasure to acknowledge and express my gratitude those who helped me along the way to completion of this thesis.

Firstly, I would like to thank my parents for all of their patience and support through the whole process of my study.

I would like to thank my advisor Assoc. Prof. Dr. Cem Çelebi for all his help, patience and detailed reviewing all of my study. Without his support and guidance, I would never have been able to complete this study.

I wish to thank the other committee members of my thesis Assist. Prof. Dr. Gökhan Utlu and Assist. Prof. Dr. Mehmet Z. Baykara for their participation and comments.

I would like to acknowledge and thank all of my colleagues and friends who helped me through the whole process of my study. Especially, I am very thankful my lab mates Erdi Kuşdemir, Damla Yeşilpınar and Batuhan Kalkan for their support and encouragement. I would also like to thank Ece Meriç for their friendship. I would like to special thank Alper Yanılmaz who supported and help me through this whole process.

I would like to thank to Eray Mustafa İnanç who always for his endless support, and patience all along.

I am thankful to Cenk Yanık from Sabancı University Nanotechnology Research and Application Center (SUNUM) for his support and help during device fabrication processes.

I wish to acknowledge using of facilities at the IZTECH Material Research Center for SEM. In addition, I would like to acknowledge the financial support from Scientific and Technological Research Council of Turkey (TÜBİTAK) for this thesis.

And last but not least, I am also grateful to my family for leading me to this stage and for their endless support during all of my life.

ABSTRACT

SELF-ORGANIZED NETWORK OF SILICON OXIDE ON EPITAXIAL GRAPHENE

In this thesis, I studied the formation and characterization of self-organized hexagonal-shaped SiO_2 wrinkle structures on epitaxial graphene that was grown on SiC substrate. Monolayer graphene was grown by annealing the SiC substrate at high temperatures under ultra-high vacuum conditions. Following the growth process, SiO_2 thin film was deposited on epitaxial graphene layer at different deposition temperatures by thermal evaporation method. We found that SiO_2 film wrinkles on epitaxial graphene. The origin of the hexagonal shaped wrinkle structures were derived from the thermal expansion coefficient difference between epitaxial graphene and SiO_2 thin film. The mesh density of these SiO_2 hexagonal wrinkle structures was controlled by changing the cooling rate of the substrate after the thin film deposition. To make a comparison, SiO_2 thin film was also deposited on CVD grown graphene and on bare SiC substrate. Unlike on the bare SiC surface, SiO_2 thin film on epitaxial graphene exhibited a self-assembled network of hexagonally shaped wrinkles due to thermally induced compressive strain between the two materials. The observed network of wrinkles were found to be comprised of line shaped primary and secondary types of protrusions with distinct topographic characteristics as determined by optical microscopy, Scanning Electron Microscopy and Atomic Force Microscopy measurements. The wrinkle to wrinkle spacing and mesh density of the wrinkle network were modified simply by changing the SiO_2 deposition temperature. Our experimental results imply that epitaxial graphene with its high chemical inertness on SiC offers a great potential to be used as a conventional substrate in the realm of thin film metrology.

ÖZET

EPİTAKSİYEL GRAFEN ÜZERİNDE KENDİLİĞİNDEN DÜZENLENEN SİLİKON OKSİT AĞI

Bu çalışmada, silisyum karbür alttaş üzerinde büyütülmüş epitaksiyel grafen üzerinde kendiliğinden düzenlenen silikon oksit ağının oluşumu ve karakterizasyonu gerçekleştirildi. Tek katman grafen, silikon karbür alttaş üzerinde yüksek sıcaklıklarda tavlanarak ultra yüksek vakum koşullarında büyütüldü. Büyütme işlemi sonrası, silikon oksit ince film tabakası epitaksiyel olarak büyütülmüş grafen üzerine farklı kaplama sıcaklıklarında termal olarak buharlaştırıldı. Yüzeyde meydana gelen kırışıklık yapısının, epitaksiyel grafen ile SiO_2 ince film arasındaki yüksek ısıl genleşme katsayısı farklılığından kaynaklandığı yapılan deneyler ile gösterildi. Bu kırışıklık yapılarının yoğunluğu ince film kaplandıktan sonraki soğutma hızı değiştirilerek kontrol edildi. Aynı zamanda epitaksiyel ve kimyasal buhar biriktirme (CVD) yöntemleri ile sentezlenmiş grafen üzerindeki kırışıklık yapısının oluşumu çalışıldı. Tek katman epitaksiyel grafen ve işlem uygulanmamış SiC alttaşın üzerinde kaplanan SiO_2 ince filmin yüzey üzerindeki davranışı incelendi. İşlem uygulanmamış SiC alttaşının aksine, iki malzeme arasında termal olarak endüklenen basma gerinimden dolayı SiC üzerinde epitaksiyel olarak büyütülmüş tek katman grafenin üzerindeki SiO_2 ince film, altıgen yapılı kendiliğinden oluşan kırışıklık ağını göstermiştir. Farklı topografik özellikler gösteren birincil ve ikincil tip yükseltilerden oluşan kırışık ağ yapısı; optik mikroskop, taramalı elektron mikroskopisi (SEM) ve atomik kuvvet mikroskopisi (AFM) ölçümleri ile karakterize edilmiştir. Kırışıklıklar arası mesafe ve yapıdaki ağ yoğunluğu SiO_2 ince film kaplama sıcaklığı değiştirilerek modifiye edilmiştir. Elde edilen sonuçlar, yüksek oranda kimyasal olarak etkisiz olan silikon karbür üzerinde büyütülen epitaksiyel grafenin ince film metrolojisi alanında kullanılmak üzere yüksek bir potansiyele sahip olduğunu göstermiştir.

TABLE OF CONTENTS

LIST OF FIGURES

Figure **Page**

LIST OF TABLES

LIST OF ABBREVIATIONS

2D……Two-dimensional

AFM……...Atomic Force Microscopy

CNT…….Carbon Nanotube

CVD…… Chemical Vapor Deposition

HF……Hydrofluoric acid

HOPG……Highly oriented pyrolytic graphite

MSM……...Metal-semiconductor-metal

OM……...Optical Microscopy

PMMA……Poly methyl methacrylate

SEM……Scanning Electron Microscopy

SiC……...Silicon carbide

SiO_2……..Silicon dioxide

TEC…….Thermal expansion coefficient

UHV……..Ultra-high vacuum

CHAPTER 1

INTRODUCTION

1.1. Wrinkle Formation

The fact that the periodic patterns are seen in nature as in biological and geological systems over wide ranging length scales is well known [1]. Said patterned structures or deformations may have a grand benefit in technology as well. People have tried to create this periodic patterns to utilize them in micro-nano technology, optical grating [2], bendable electronics [3] and especially lithographic techniques. Complete execution of these applications necessitates full comprehension of the part which sheet properties and substrate geometry for delamination play in the equation.

Wrinkle networks have been observed in various substrates. Thermal vibrations, edge instabilities, strain in two dimensional crystals induce wrinkles or ripples to form on the substrate. Distinctive deformation in graphene on various substrates are wrinkles formed due to the variant thermal expansion coefficients between substrate and graphene, and also arising from the lattice mismatch between thin film layer and substrate [4]. In literature, the out of plane deformations as ripples and wrinkles depend on the size and structure characteristics of the substrate [5]. Furthermore, these corrugations on graphene can modify its transport properties [6], create polarized carrier puddles [7], increase chemical reactivity [8], induce pseudomagnetic field in bilayers and change surface properties [9]. In addition to all these characteristics, wrinkles play an important role in the changing wettability and optical transmittance of graphene [10]. Consequently, governance of their macroscopic ordering along with a systematic characterization is desired to successfully implement the graphene in the technological aspect.

Furthermore in graphene, wrinkles have been observed on the other types of layered materials. For instance; wrinkle formation on crystalline large area graphene grown on a poly-Ni substrate by using CVD as a result of the thermal expansion coefficient between Ni substrate is observed by using optical microscopy (Figure 1) [11]. Wrinkle density can be changed by means of optimizing the growth temperature, gas mixing rate and growth rate.

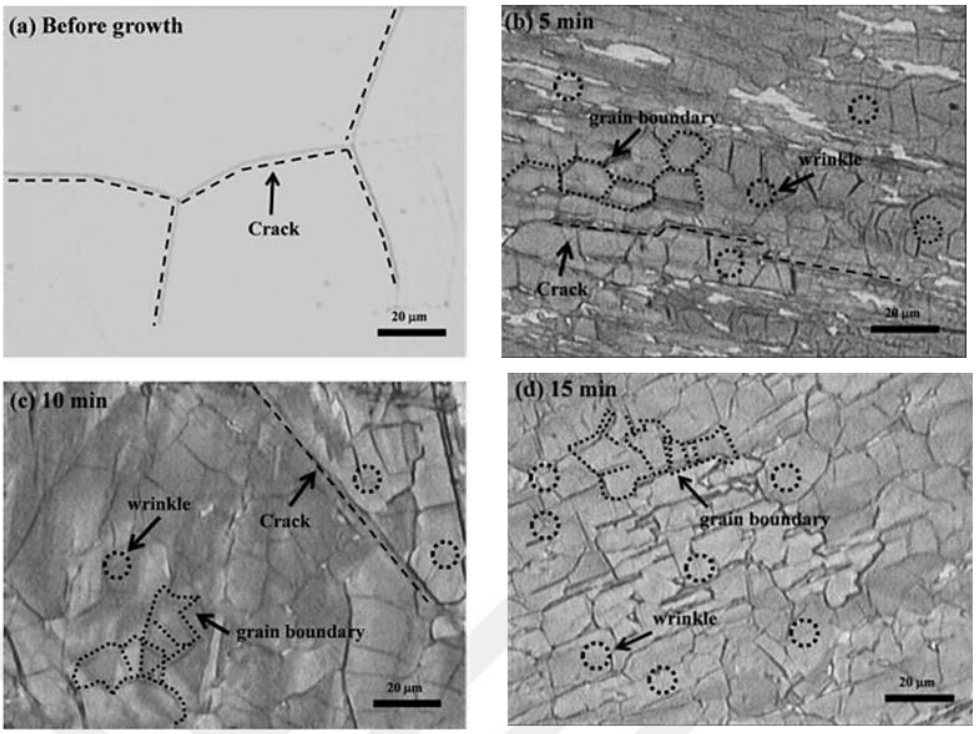

Figure 1. Graphene wrinkle formation on poly-Ni substrate (a) after reduction without growth after (b) 5 min, (c) 10 min and (d) 15 min of growth [11].

Another study about the nanofold formation is that the deposition of Cu with some time on VSe_2 layered crystal prepared by the chemical vapor deposition technique is characterized by Scanning Electron Microscopy (SEM) (Figure 2) [12]. The mesh size of the network changes between 400 and 800 nm and these nanostructures meet at 120°. It is claimed that it is possible to transfer this nanofold structures with linear cavities. Spiecker et al. have stated that these wrinkles form due to two main reasons: diffusing into the top layers of the layered crystal and creating an interposition phase. And therefore a lattice expansion forced by the rigid substrate, causing the building up of compressive biaxial strain and stress in the intercalation layer (self-assembled nanofold) accompanies this phase. The relaxation of layer strain in the mesh zone due to the lateral displacement of the layered materials against the folding zone causes the wrinkle to form.

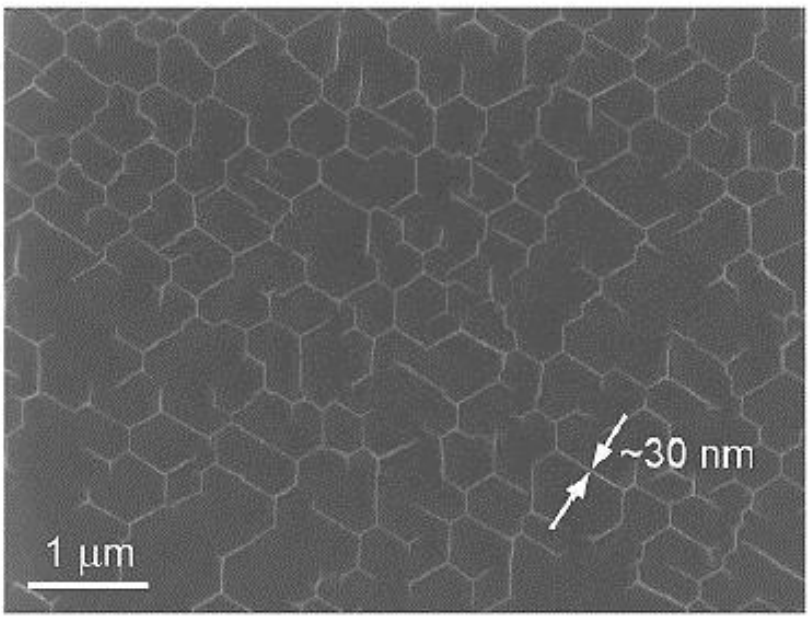

Figure 2. SEM image of self-assembled hexagonal network of nano-fold formed on VSe_2 surface [12].

The interaction between the graphene layer and the substrate substantially affects the occurrence of the ripples and wrinkles. The contrary thermal expansion coefficient between graphene and substrate contributes to the horizontal displacement of the graphene sheet which stems from the flexural phonon modes while the in-plane phonons contribute only a little [13]. The dimensions of the ripples formed on the mechanically exfoliated graphene are 1 nm (height) x 10-25 nm (lateral) [14]. These wrinkle structures have been explained as the formation of an electron-hole puddle, decreased carrier mobility, and increased chemical reactivity. Wrinkles also appeared on transferred graphene surfaces which were grown by chemical vapor deposition method. These wrinkles generally are 2-15 nm in height and 20-100 nm in width [14]. The wrinkle formed on the CVD graphene is wider than the mechanically exfoliated one influencing graphene samples in regard to their physiochemical properties. Researches have reported that this highly ordered honeycomb pattern forms on the thin layered crystalline film on Al_4C_3 and carbon synthesized on a sapphire c-plane substrate with chemical vapor deposition method [15]. After increasing the annealing temperature up to some point, the thin film begins to appear as a two dimensionally periodic pattern and characterized by optical microscopy (Figure 3). This formation of hexagonal patterns are the result of the relaxation of strain during the annealing process.

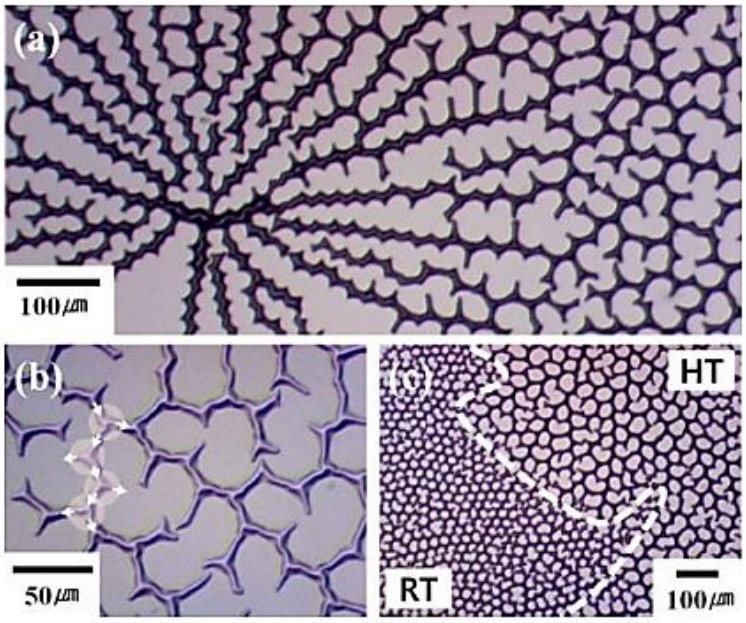

Figure 3. Optical microscopy images of formation of hexagonal pattern structures (a) from center of the substrate (b) branch connection of hexagonal pattern (c) boundary between pattern with room temperature (RT) and high temperature (HT) at 1000°C.

The aim of this thesis is to demonstrate a new approach to create and tune mesh like wrinkle patterns without using multi-staged lithographic techniques. We indicate that the self-assembled hexagonal network forms to minimize biaxial compressive strain energy. This is caused by the effect of compressive stress in an evaporated thin SiO_2 film deposited onto epitaxially grown graphene substrate. Lateral strain produced upon cooling of graphene grown in epitaxially growth on SiC substrate causes in hexagonal shaped wrinkles. Such phenomena would be used in a great number of applications, including especially lithography without any inconvenient chemical processes [16, 17, 18].

1.2. What is Graphene?

Graphene is a rising material which consist of honeycomb lattice structure of sp^2 hybridization of carbon atoms. This two-dimensional (2D) allotrope of carbon atom plays an important role since it is the origin for the considering of the electronical, mechanical and optical properties in other allotropes. Graphene is a one atom thick, zero band gap semiconductor material. It is a highly wanted material in carbon based nanomaterial

family with the excellent properties. Today, graphene is a potential member of next generation nano devices with unique properties in photonics, optoelectronics, [19] biomedical applications [20] such as; transistors [21] supercapacitors [22], drug delivery [23] and nano-lubricant [24].

In recent years, carbon based materials have been a focal point of experimental studies. Not only graphene, but also allotropes of carbon atoms have drawn a great deal of attention at least as much as graphene. Carbon atom is capable of forming many allotropes due to its valency. The most famous known allotropes of carbon are diamond and graphite. In time, many more types of allotropes of carbon atoms have been discovered. Fullerenes are zero dimensional (0D) materials that form spherically with discrete state energy levels. Carbon nanotubes (CNTs) are another type of allotrope of graphene which are one dimensional (1D) materials obtained by folding graphene throughout a given direction and reconnecting the carbon atoms with a cylindrical structure. Graphite, takes the place of stack of graphene layers, a three dimensional (3D) allotrope of carbon atom. This two dimensional (2D) sheet sp^2 hybridized carbon atoms show excellent properties not only scientifically but also technologically (Figure 4).

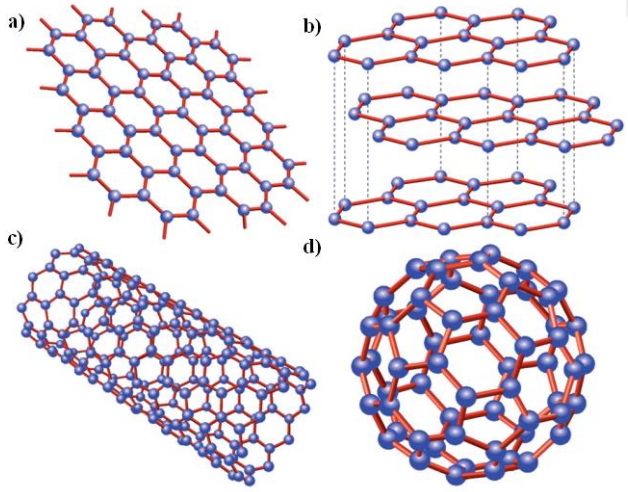

Figure 4. Schematic view of allotropes of carbon atoms (a) graphene (b) graphite (c) nanotube (d) buckminsterfullerene (C_{60}) [25].

One atom thick graphene was first studied as long ago as 1947[26]. Experimental researches of graphene have been started with discovering of graphene by Geim and co-workers, first exfoliated graphene from graphite in 2004. This study got the Nobel Prize

in physics for their pioneering work and graphene has started to be the breakout star of the year. The quantum hall effect at room temperature [27], high charge carrier mobility [28] and extremely high thermal conductivity [29] where the initial studies and researches. All such effects are fundamental elements for the designing of the electronic devices when compared to silicon based devices and are of high interest to the scientists.

1.3 Properties of Graphene

1.3.1 Structure of Graphene

As mentioned before, graphene is a two dimensional semiconductor material which consists of carbon atoms with a hexagon shape. The distance between carbon atoms is 0.142 nm [30]. Graphene is a single two dimensional hexagonal sheet of carbon atoms and consist of honeycomb lattice structure as shown in Figure 5. This honeycomb lattice is not a Bravais lattice because the distance between two neighboring sites is different.

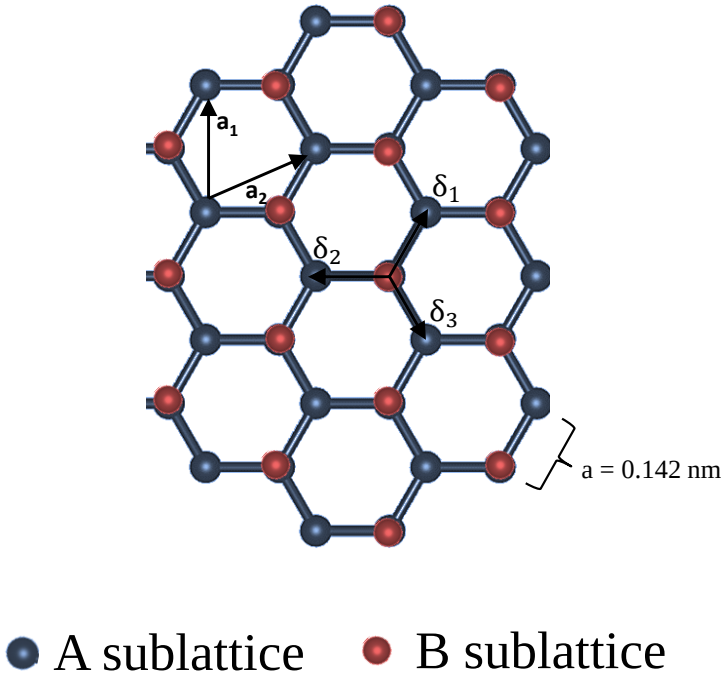

Figure 5. Honeycomb lattice structure of graphene. δ_1, δ_2 and δ_3 are the vectors with connect to carbon atoms.

The unit vectors in real space are indicated as a_1 and a_2;

$$a_1 = a\left(\frac{3}{2}, \frac{\sqrt{3}}{2}\right) \text{ and } a_2 = a\left(\frac{3}{2}, \frac{-\sqrt{3}}{2}\right) \quad (1.1)$$

The three vectors which connect a side on the A sublattice on the B sublattice are given by;

$$\delta_1 = \frac{a}{2(\sqrt{3}e_x + e_y)} \qquad \delta_2 = \frac{a}{2(-\sqrt{3}e_x + e_y)} \qquad \delta_3 = -ae_y \quad (1.2)$$

and the reciprocal lattice vectors are;

$$b_{1=} \frac{2\pi}{a}\left(\frac{1}{3}, \frac{\sqrt{3}}{3}\right) \text{ and } b_{2=} \frac{2\pi}{a}\left(\frac{1}{3}, \frac{-\sqrt{3}}{3}\right) \quad (1.3)$$

Graphene consist of crystalline allotrope of carbon atoms which have 6 electrons in group 4A in periodic table. Bonds in graphene has sp^2 hybridization. There are three in-plane sigma (σ) bonds which are s, p_x and p_y. These bonds are extremely strong and form the structural stability of the hexagonal structure. Partially filled p_z orbitals (π orbitals) perpendicular to the plane are responsible for the electron conduction (Figure 6). On the other hand, there is sp^3 hybridization between graphene sheets, such as graphite. Therefore, between the layers out of plane π orbitals give rise to weak van der Waals forces. Due to this fact, it is relatively easy to obtain monolayer graphene from graphite flakes with the exfoliation method.

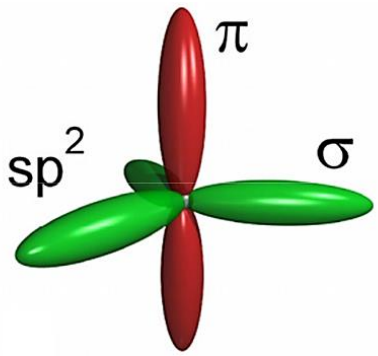

Figure 6. Schematic view of orbital structure of graphene [31].

1.3.2 Mechanical Properties of Graphene

Experimental studies indicate that graphene shows excellent mechanical properties when compared to other 2D materials such as MoS_2, WSe_2 [32]. Also, recent mechanical experiments have shown that graphene is the strong material measured so far due to the in plane σ bonds [33]. The mechanical properties of graphene under tension have been investigated extensively using both experiments and atomistic simulation methods[34]. There is weakly coupled by van der Waals forces for each graphene layer, between two carbon atoms exist strong covalent bonding. It is few hundred times stronger than steel. In addition to this, Young Modulus of graphene was recorded $E = 1.1 \pm 0.1$ TPa [33] and breaking strength is 42 N/m which gives that graphene is the strongest material ever measured [33].

1.3.3 Electronic Properties of Graphene

Graphene is a zero band gap semiconductor due to linear Dirac point. The conduction band and valance band connect at the corners of hexagon which is called Dirac point (Figure 7). Because of the gapless material, electrons near the Fermi level act like as if they are massless. Fermi level should be around the Dirac point, in which the charge carriers solely go through a linear dispersion, for an intrinsic or lightly doped graphene. This linear dispersion is called the Dirac cone because of the fact that it is defined by the relativistic Dirac equation. The Dirac electrons can be kept under control by applying external electric and magnetic fields or altering the sample. It is, as aforesaid, due to the fact that the structural flexibility of the graphene can be seen in its electronic characteristics. In accordance with the Pauli principle, these bands have a filled shell and hence form a valence band. The p-orbital, which remains unaffected and is vertical to the planar structure, can form a covalent band with the neighboring carbon atoms. And since every p orbital has one extra electron, the π band is half filled [36].

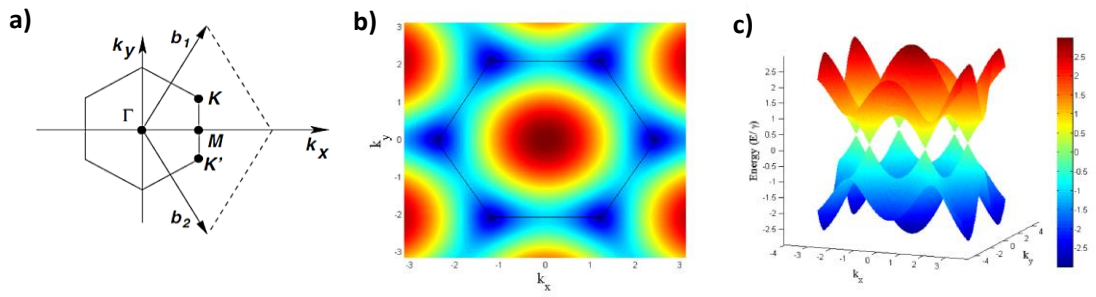

Figure 7. (a) Reciprocal lattice vectors of graphene[36] (b) 1st Brillouin zone of graphene (c) The band structure of graphene with E=0 (Dirac point) [37].

The band structure of graphene can be calculated from reciprocal lattice in Figure 7 (a) by using tight binding approximation [38]. Tight binding calculations for the graphene are described by;

$$E(k_x, k_y) = \pm\gamma \sqrt{1 + 4cos^2\left(\frac{k_y a}{2}\right) + 4\cos\left(\frac{k_y a}{2}\right)\cos\left(\frac{k_x\sqrt{3}a}{2}\right)} \qquad (1.4)$$

where γ $(\sim 2.7\ eV)$ and a indicates nearest neighbor hopping energy and a (2.46 Å) the lattice constant of graphene respectively.

According to the tight banding calculation, graphene has no band gap. This is a result of linear dispersion relation of graphene. As seen in Figure 7 (c) K and K' are the high symmetry points (also called Dirac points) of graphene and at this points graphene electrons and fermions act as a massless particles. The charge carriers in graphene mimic relativistic particles with zero rest mass and have an effective 'speed of light' which is $c \sim 10^6$ m/s [28]. At absolute zero, there are no charge carriers present near the K and K' point which is called charge neutrality point.

In addition, graphene has high mobility (μ) even in room temperature [28]. An extraordinary trait of graphene is that μ preserves its high level even at the highest electric-field-induced concentrations; furthermore, it looks unaffected by chemical doping. This means ballistic transport on a sub-micrometer scale at 300 K. A room-temperature ballistic transistor has been a tempting dream of electronic engineers to this day. The studies carried out concerning the single layer graphene have revealed the distinctive characteristics of graphene and suggested the probability of application of graphene in a vast number of devices [39], especially sensors [40], transparent electrodes [41] and solar cells [43] reinforced composites.

1.3.4 Optical Properties of Graphene

It is possible to measure the absorption spectrum of graphene due to the simple electronic band structure of graphene. Monolayer and bilayer graphene are zero band gap two dimensional semiconductors. Therefore, the dimensionality effects can be studied in the unique substance. In the infrared limit absorption coefficient is exactly $\pi a \sim 2.3 \pm 0.10\%$ [44], where $a = e^2/\hbar c$ is the fine structure constant, and the correction to this number in the visible range of the spectrum less than 3% [45]. It can be explained by constant conductivity in the visible range. Because of the linear dispersion relation behavior, it has been shown that

$$\varepsilon = \pm \hbar v_f k \tag{1.5}$$

where ħ is the Planck constant , v_f (~ 10^8 m/s) is the Fermi velocity and k is the wave vector [46]. The positive sign and negative sign on the right-hand side of the equation correspond to the upper part of the Dirac cone (the conduction band) and the lower part of the Dirac cone (the valance band), respectively.

Ni/Au, Ti, TiW and ITO have been performed as a transparent electrode which will collect photo-generated charge carriers especially in optoelectronic and photovoltaic devices in literature during the last decade. Unlike other transparent contact materials, graphene is seen to be able to transmit > 90% of the light in the wavelength range between 200-400 nm [41]. When we combine this high UV transmission level with the zero band gap property, graphene becomes a likely good candidate as a transparent and conductive electrode for such devices. It was recently indicated that a multilayer graphene template, which was grown by chemical vapor deposition (CVD) technique, could be used as a transparent Schottky electrode for GaN based metal-semiconductor-metal (MSM) type UV sensor [47].

1.4 Graphene Production Methods

1.4.1 Micromechanical Exfoliation

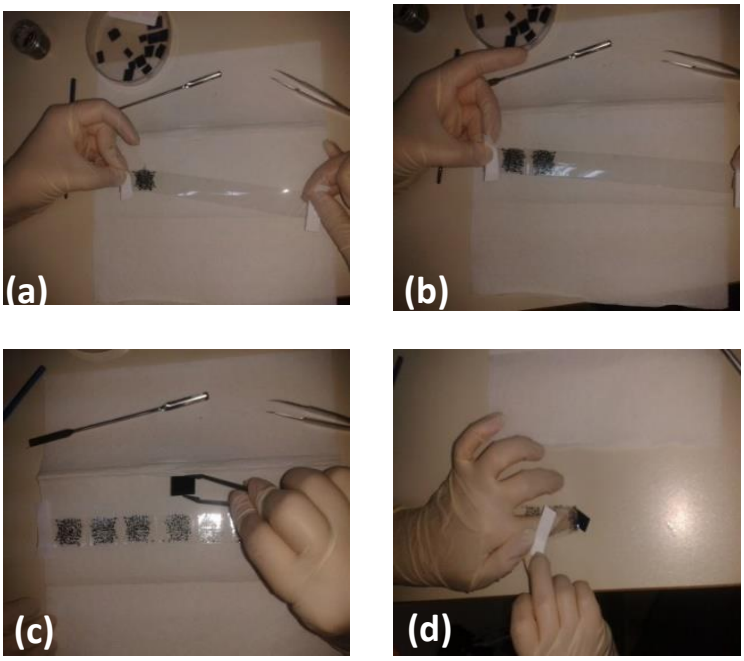

Figure 8. The illustrative procedure of mechanical exfoliation method from HOPG flakes to graphene on 300 nm Si/SiO_2 substrate.

Up to now, a large number of methods have been proposed to produce graphene. Graphene was first discovered with using micromechanical exfoliation method in 2004 by Andre Geim and Konstantin Novoselov who got Nobel physics prize in 2010. This method is somewhat simple; with using scotch tape Highly Oriented Pyrolytic Graphite (HOPG) flakes peel of small graphene particles (Figure 8). In this method, graphene is exfoliated from the bulk graphite layer by layer which is also known scotch tape method. The resistance to be overcome is the Van der Walls attraction between graphene flakes [48]. Decoupled graphite particles is transferred to 300 nm SiO_2 covered Si substrate for creating contrast difference by characterizing with optical microscopy. By using this method, it is possible to observe high carrier mobility even at room temperatures in exfoliated graphene flakes [49]. However, with using these technique, it is possible to obtain few or more layer graphene films up to 10 μm in size [50] and number of layer is not controllable. In addition to this, with this method, obtained graphene flakes are very

defective. Therefore, this method is not scalable meaning one cannot make large areas of graphene which are required for the fabrication of electronic devices.

1.4.2 Chemical Vapor Deposition

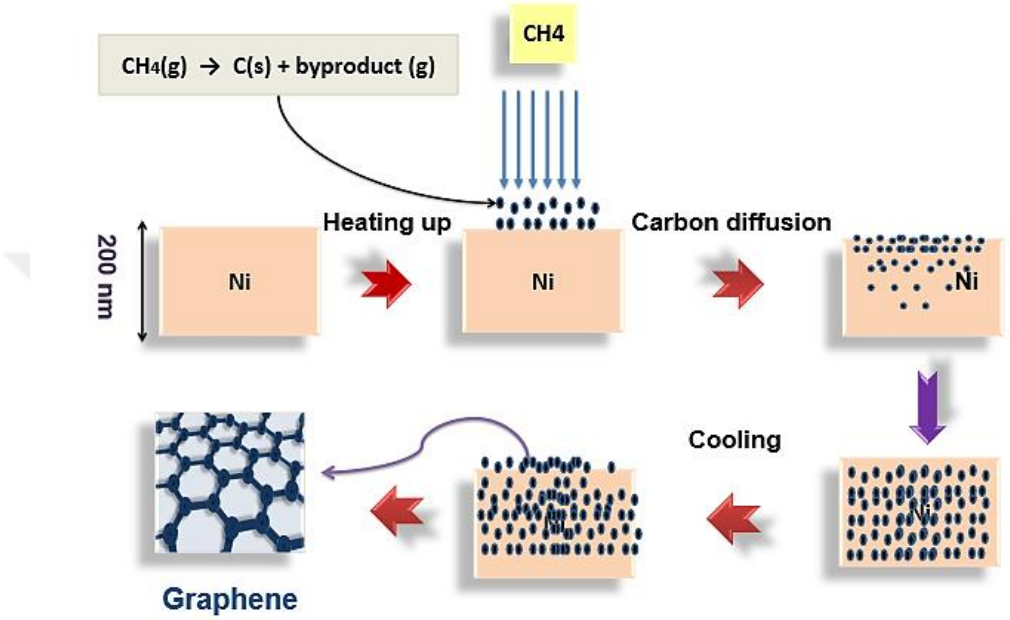

Figure 9. Schematic representation of CVD graphene synthesis method on Ni thin film [51].

As mentioned in literature [52,53] , chemical vapor deposition (CVD) is the most common method for synthesis large area graphene. Graphene production is based on the deposition of carbon atom on metal substrates such as Ni, Cu, Ir and Pd (Figure 9). This transition metals act as catalyst for transforming hydrocarbons into graphitic materials [54]. With this technique, carbon source gases such as C_2H_2, C_2H_4 and CH_4 etc. are deposited onto the metal substrates in CVD reactor with relatively high temperatures (800-1000^oC) depending on the carbon sources, at low pressure (order of mTorr) or atmospheric pressure. Carbon solubility changes with the used transition metals as given above. For instance, nickel has higher carbon solubility with respect to copper [52,55]. Therefore, cooling process plays an important role as well as growth or annealing process for graphene growth by using CVD. During the graphene synthesis process, precursors contain carbon based gases that react on the transition metal surface under the ambient

environment. Also, it is well known that for controlling number of layer of graphene with CVD system, the solubility of the carbon in transition metal plays a critical role [52]. Synthesis graphene with CVD method, shows mobility of the order of 3000 cm^2/Vs [52], 90% transmissivity [56] and 280 Ω sq [57]. Although with this method, it is possible to obtain large area graphene with respect to sample size, it is limited to use in electronic device applications due to the metallic substrate and it needs to be transferred to insulating substrates. During transfer process, to create unavoidable defects to the graphene is inevitable and this changes the electronic properties. Another property of CVD graphene method is that forming sheet is inherently polycrystalline because of the grain boundaries. This results in poor electronic properties [58].

1.4.3 Epitaxial Growth of Graphene on SiC Substrate

Mechanical exfoliation is a shortcut method for obtaining single or few layer graphene. However, with this method obtained graphene flakes will be both small size and cannot be used in technological applications like transistors or sensors. In addition to this, with CVD method it is possible to produce large area and few layer graphene but then during transfer processes lots of chemicals should be used. Since these chemicals cannot be removed completely from the sample surface [59] after transferring to other substrates, they can be caused to be some problems in device processing.

Epitaxial graphene growth method used to produce ultrathin epitaxial graphite films by sublimation of Si from SiC substrate under ultra- high vacuum (UHV) conditions. With this efficient technique, it is possible to grow epitaxial single and multilayer graphene films in ultra-high vacuum by thermal decomposition of SiC at the range of ~1350-1400℃ regime [60–62]. Epitaxial multilayer graphene films have been extensively characterized by surface analysis tools, electronic transport experiments, infrared spectroscopy, and other techniques [63–65].

1.5 Strain –Stress Mechanism on Thin Films

Stress is force per unit area that is acting on a material. In thin films, stress have three primary origins which are intrinsic, thermal and mechanical. Thin films are stressed even without the application or externally imposed forces and characterized by residual stress. Intrinsic and thermal stresses are often referred to residual stress. As opposed to thermal stress, stress which arise from mechanical reasons is called mechanical stress. Most mechanisms producing intrinsic stress result in a change in volume which then generate stresses due to the constraint of the substrate or other layers. Intrinsic stresses arise from deposition process such as sputtering, spin coating or spraying and deposition temperature can be low, high or room temperature. As distinct from thermal stress, intrinsic stress presents at the deposition temperature. On the other hand, thermal stresses can result from changing in temperature when the film and substrate have different thermal expansion coefficient (α). And also, when the sample temperature different from the deposition temperature, the residual stresses comprise both intrinsic and thermal contributions.

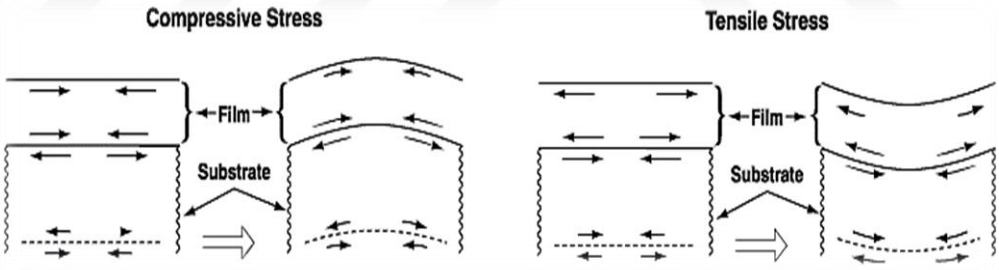

Figure 10. Schematic representation of compressive and tensile stress mechanism on thin film.

The residual (internal) stress can be compressive and tensile. A piece of solid is under stress when during temperature changes occurring the deposition different material. During tensile stresses, atoms are further apart they would be in the annealed state, in addition to this, in the case of compressive stresses, the atoms are closer together than they would be in the annealed state. The film stress depend on film thickness, Young's modulus of thin film, morphology and density of the thin film. As seen in Figure 10, films under compression will try to expand and if the substrate is thin, the film will bend the

substrate with the film being convex side. On the other hand, if the film is under tensile stress the film will try to contract to substrate so the film is on the concave side.

Upon cooling, substrate and film shrink by some factor given by their thermal expansion coefficient (α) and it comes straight from bonding potential. The thermal expansion coefficient α is defined as the rate of uniaxial strain with temperature:

$$\alpha\ (T) = \frac{d_{\epsilon_x}}{d_T} \tag{1.6}$$

where T defined as temperature. The unit of α is Kelvin^{-1} (K^{-1}). Since $\alpha\ (T)$ is defining a dimensionless strain per Kelvin, $\alpha\ (T)$ is usually in a range of 10^{-6}-10^{-7}.

For a moderate temperature $\alpha\ (T)$ is a constant of the material. Therefore, for a finite temperature change ΔT,

$$\epsilon_x(\mathrm{T}) = \epsilon_x(\mathrm{T_0}) + \alpha_T \Delta T \tag{1.7}$$

where $\epsilon_x(\mathrm{T_0})$ is the strain at the original temperature $\mathrm{T_0}$, and ΔT equals to $\mathrm{T\text{-}T_0}$.

When a thin film material is attached to the substrate, the thermal behavior is more complicated. The thin film is much thinner with respect to the substrate in a stress-free state at deposition temperature $\mathrm{T_d}$ and then cooled to room temperature $\mathrm{T_r}$. The substrate contracts according to the own thermal expansion coefficient and the film is attached to the substrate. Therefore, thin film must bond by the same amount as the substrate. Then, the strain of the substrate is,

$$\epsilon_s\ = \ -\ \alpha_{T_s} \Delta T \tag{1.8}$$

where $\Delta T = T_d - T_r$, α_{T_s} is the linear expansion coefficient and E is the Young's modulus of the substrate. If the thin film were not attached to the substrate, then strain is given by,

$$\epsilon_{f,free}\ =\ -\ \alpha_{T_f} \Delta T \tag{1.9}$$

where α_{T_f} is the linear expansion coefficient of the film. Yet, because of its attachment to the substrate, the actual strain in the thin film must be equal that of substrate ($\varepsilon_f\ =\ \varepsilon_s$). Then,

$$\epsilon_{f,attached}\ =\ -\ \alpha_{T_s} \Delta T \tag{1.10}$$

Therefore the thermal mismatch strain is defined as an extra strain and is given by,

$$\epsilon_{f,mismatch}\ =\ \ (\alpha_{T_f} -\ \alpha_{T_s}) \Delta T \tag{1.11}$$

The film can succeed the state of strain is to develop an in-plane biaxial stress which is given by,

$$\sigma_{f,mismatch} = \left(\frac{E}{1-\upsilon}\right)\ \epsilon_{f,mismatch} \tag{1.12}$$

where υ is the Poisson's ratio of the thin film [66].

1.6 Wrinkles on Graphene

Whether it is a macroscopic system such as a geological plate or a microscopic system such as a thin film, deformation of a system is known to introduce a pattern [1]. This induced pattern is expected to be of great use in the field of technology if harnessed and controlled appropriately, due to the obvious fact that today's micro and nanotechnology are only achievable by the patterning processes [24,67]. Stress in thin films is known to cause yield and affect actual device efficiency to substrate especially optoelectronic devices [1]. In addition to this, wrinkle structures are part of the many electronic properties of material including electron-hole puddles [68], band gap engineering [69] and pseudomagnetic field in bilayers [70].

Thin films are often subject to a considerable amount of strain when they are deposited on compliant substrates due to differential thermal contractions and/or to a large lattice mismatch between the respective materials. The main causes of these instabilities on the thin film surface are compressive [71] and tensile [72] stress. The inherent strain, released upon cooling of incompatible film/substrate stack from the process temperature, can yield mechanical instabilities in the uppermost surface layers. Differently from their 1D (one-dimensional) and 0D (zero-dimensional) counterpart, 2D nanomaterials, such as graphene, exhibit surface corrugations like wrinkles, ripples and cracks. As graphene is a thin material, it is easily susceptible out of plane deformations that causes to formation of wrinkles because of the stress relaxation (Figure 11 (a)). This relaxation generally caused by thermal expansion coefficient difference between substrate and thin film layer during the annealing process [14,17]. According to the theoretical calculations, the localized wrinkles in graphene are preceded by distributed ripples of very small amplitude upon uniaxial compression (Figure 11 (b)). By intentionally straining the substrate uniaxial, lateral strain is transmitted to graphene perpendicular the strain direction [73]. Besides the thermal expansion coefficient difference between the thin film and the substrate, surface

friction acting on the thin film is effected to form wrinkle structure. Graphene interacts with the substrate non-covalently and this causes perpendicular adhesive forces and tangential frictional forces opposing sliding (Figure 11 (c)). The thin film adhesion to the substrate is related to the substrate friction properties. The increased the adhesion may be attributed to a larger contact area and this causes to occur wrinkle structure on thin film surface [74].

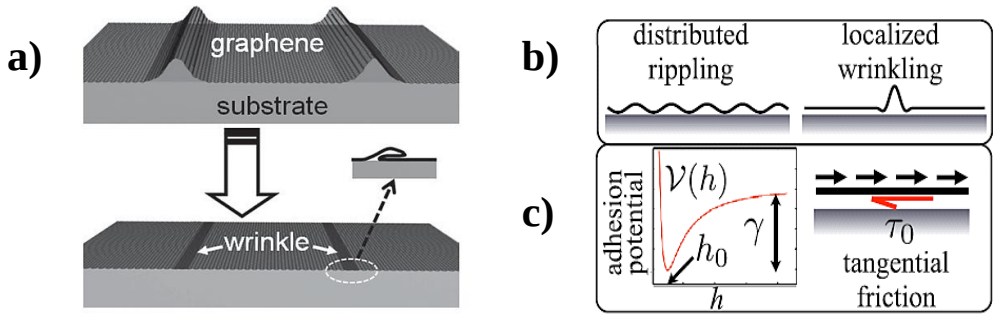

Figure 11. (a) Schematic of wrinkle formation on the substrate[75]. (b) During compression, schematic of distributed rippling and localized wrinkling (c) Upon graphene interact with substrate and through adhesion energy. Modeled as dry friction with interfacial shear strength[76].

The common occurrence of a mesh-like ridge structure has been observed in epitaxial graphene on SiC substrate. Ridges may likely form during cool down when wrinkles in the few layer coalesce. Briefly, after epitaxial graphene growth at high temperature, anisotropic compressive stress progresses upon cooling due to the differential thermal expansion coefficient between SiC and the epitaxial graphene. In the case of responding to this compressive stress, the film deforms and buckles, forming ridges or wrinkles. In Figure 12 (a), AFM image of wrinkle structures on few layer epitaxial graphene after annealing of SiC substrate at high temperature (~ 1600 ℃) was investigated. The ridges are not uniform height and contain a number of localized ridge nodes. The height of the primary ridges is about 10-15 nm and secondary ridges has lower height which is about 2-10 nm height [77]. Furthermore, wrinkle structure on epitaxial graphene has been observed with AFM measurements (Figure 12 (b)). The height of this structures is less than 2 nm and they are typically separated by few hundred nanometers.

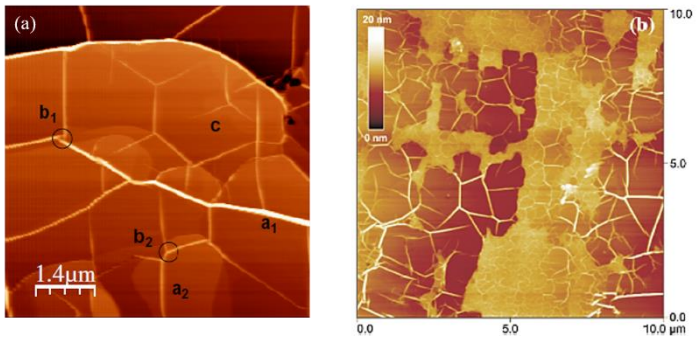

Figure 12. (a) AFM image of few layer graphene grown on 4H-SiC substrate with ~ 2 µm x 2 µm ridge network size. The labels a_1 and a_2 indicates primary ridges, ridge nodes are labelled as b_1 and b_2 and c is the secondary ridge[77]. (b) AFM image of wrinkle network after graphene growing at T = 1600 ℃ for 40 min [78].

Similar to observed in epitaxial graphene, the wrinkle structures can be found also on exfoliated graphene and CVD grown graphene on SiO_2 substrates. However, these wrinkles are about 10 nm width and 3 nm height [79]. Because of the non-controlling number of layer graphene flakes and small size, it is hard to control the formation of these wrinkle structures. The studies conducted on CVD grown graphene also exhibits ripples on the surface, which arise from the thermal expansion difference between the metal and the graphene grown on the surface [9]. The metal contracts more than graphene during post cooling process, thus leaving an excess area of graphene which absorbs the strain energy by mechanical deformation and forms a wrinkle. While the flexural phonon modes play the main role in the horizontal displacement of the graphene sheet, the in-plane phonons are found to have a very little contribution. This phenomenon is thought to be the main reason for graphene's negative thermal expansion coefficient. The opposite polarity relationship between graphene and metal gives rise to high densities of wrinkles in CVD grown graphene.

CHAPTER 2

SILICON CARBIDE AND EPITAXIAL GRAPHENE

2.1 Crystal Structure of SiC

Silicon carbide (SiC) has been an accidentally discovered by Edward G. Acheson in 1890 while synthesizing diamond. SiC occurs in nature in meteorites in a small amount. SiC is used in industry as an abrasive and cutting tool. Also SiC is utilized in the field effect sensors for optoelectronics [80].

Silicon carbide is composed of tetrahedral of carbon and silicon atoms with strong bonds in the crystal lattice. The distance between C and Si atom is approximately 1.89 Å [81]. SiC resists relatively high temperatures (~ 2829 ℃) because of the little or no grain boundary impurities which gives the strong material. Also it has relatively high thermal conductivity (3.3 times higher than that of Si at 300K) [82] coupled with low thermal expansion (for 4H polytypes 4.06 x 10^{-6} /℃ with a temperature range 20 ℃ to 1000 ℃) [83] give this material exceptional thermal shock resistant qualities. In addition to all these properties, SiC stable to chemical attack at temperature, and robust at high temperatures which make SiC an ideal candidate for wafer tray supports, ion implantation, supercapacitors, sensors, high power and high frequency applications [82,84,85]. The electrical conduction of the material has led to its use in resistance heating elements for especially heating systems. Because of all these several advantages over other wide band gap semiconductors, SiC is well suited for many technologic applications [86]. Indeed, SiC nanomaterial has been a rising star from an increasing number of published research works on them.

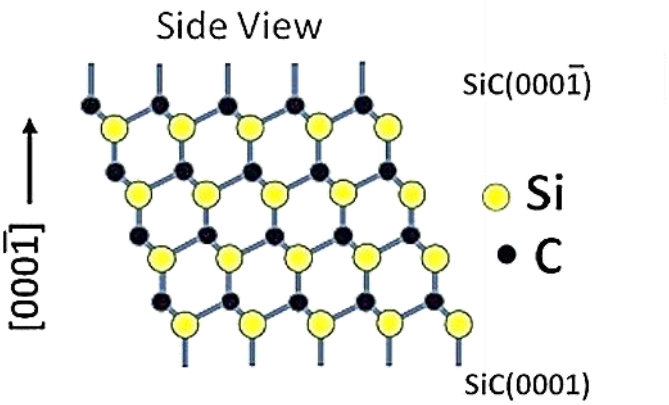

Figure 13. Representation of 6H-SiC of polar faces C (000-1) face and Si (0001) face.

SiC is a common wide band gap semiconductor whose band gap energy changes in the range between 2.0 eV to 7.0 eV [82]. Because of this fact SiC operates at extremely high temperature and high voltage. The Si-C bond length is 1.89 Å and the distance between two bilayers is 2.52 Å [87]. SiC consist of two different terminated face. The SiC (0001) surface is called Si-face which is terminated by Si atoms, while the SiC (000-1) surface is called as C-face which is terminated by C atoms (Figure 13). These two different surfaces shows different physical and chemical properties with respect to growth of graphene [88].

(a)

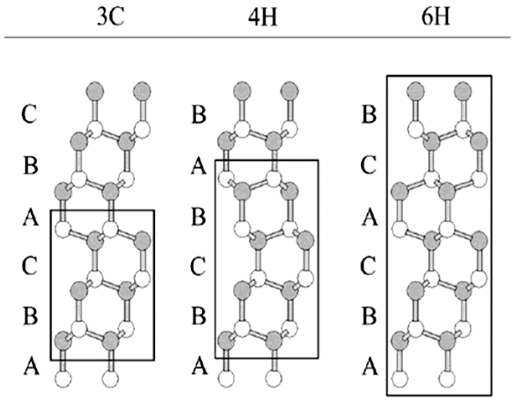

(b)

Polytype	Stacking sequence	Lattice constant (Å)	Band Gap (eV)
3C-SiC	ABC	4.36	2.3
4H-SiC	ABAC	3.08	3.3
6H-SiC	ACBABC	3.08	3.0

Figure 14. (a) Illustration of some main polytypes of SiC (b) and their properties [89].

SiC has more than 250 polytypes but few of them are commonly used (Figure 14 (a)). Depending on polytypes, SiC shows two different type of crystal structures as seen in Figure 14 (b). For example, α- SiC has hexagonal crystal structure and it forms out temperatures greater than 1700 ℃. On the other hand β-SiC has zinc blende crystal structure and forms below 1700 ℃. According to different types of stacking sequences and crystal structures, it is shortened with numbers like 2, 3 or 4 and H (hexagonal) and C (cubic), respectively. Furthermore, SiC is considered to be one of the few lightweight covalently bonded ceramics. The theoretical density of β-SiC is only 3.16 g/cm^3 and that of α-SiC (for 6H) is 3.21 g/cm^3. Combining its lightweight and strong covalency with other properties, such as low thermal expansion coefficient and high thermal conductivity, strength and hardness, make SiC a promising ceramic for the replacement of conventional metals, alloys and ionic bonded ceramic oxides.

2.2 Growth of Epitaxial Graphene on SiC Substrate

Historically, graphene has been reported as a monolayer graphite which was known since 1994 [90]. Van Bommel et al. was the first study of epitaxial graphene on SiC substrate in ultra-high vacuum [91]. This method was verified by different surface scientists. The small lattice mismatch between substrate and graphene shows that SiC is a quite suitable substrate to grow graphene.

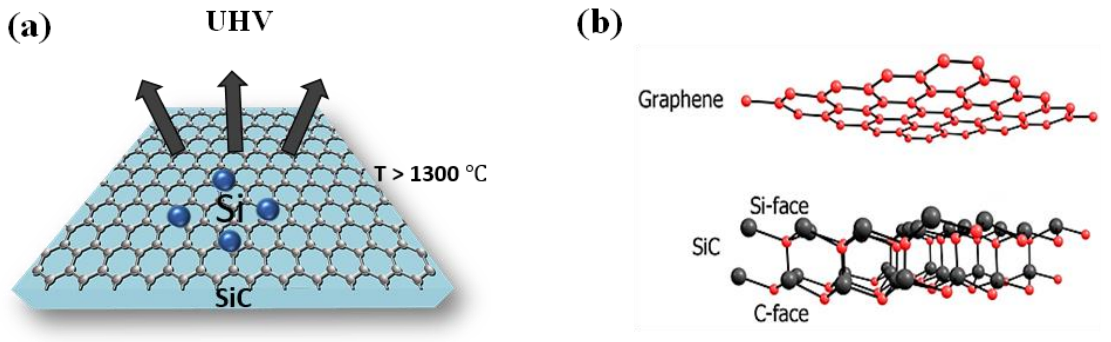

Figure 15. (a) Illustration of growth of epitaxial graphene under UHV condition (b) Schematics of Si and C-faces of SiC crystal.

As mentioned in previous chapter, epitaxial graphene growth is a method which is based on the sublimation of the Si-atoms at high temperatures e.g. above 1300 ℃ from SiC substrate under ultra-high vacuum conditions (Figure 15 (a)). The left behind C-atoms create honeycomb lattice on the SiC surface. One third of C atoms in reconstruction layers has covalent bonds to underlying Si-atoms of the topmost layers of SiC. This constructed layers has shown graphitic properties and structure. However, it strongly interacts with the substrate and leads to electronic properties which is different from an isolated graphene layer [92].

Growth process starts at elevated temperatures which is higher than evaporation temperature of silicon atoms. After evaporating Si atoms from the SiC surface, covalent bond between Si-atoms and the substrate is broken, this bond become free which constitute carbon atom to consist of sp^2 hybridization. The sublimated Si-atoms leave behind three dangling bonds of carbon atoms where in the topmost layer of the SiC these bonds form interface layer with connecting each other. Furthermore, the next graphene layer occurs in the same manner and interacts with the interface via van der Waals forces. This new graphene layer positions different with respect to two terminated faces (Figure 15 (b)). For the Si-terminated face of SiC (0001), the layers show good AB stacking order of graphene. However, for the C-terminated face SiC (000-1), there is no formed reconstruction layer because of the surface polarity and the dangling bond properties. This causes a weak interaction between graphene and substrate which can be explained by azimuthal asymmetry. Therefore, growth mechanism shows discrepancy with respect to Si an C terminated faces [93,94].

2.2.1 Growth of Graphene on the Si-face of SiC

Graphene growth on the Si-face of SiC substrate under ultra-high vacuum has been studied by many researchers. As mentioned before, there is a complex interface layer between graphene and SiC for the growth on the Si-face. On Si-terminated face of SiC (0001), $(6\sqrt{3}\ x\ 6\sqrt{3})$ R30° (in short $6\sqrt{3}$) reconstruction is observed and this interface structure acting as a template for the formation of graphene ensuring well-ordered graphene on that surface [95,96]. Si-face graphene is epitaxial with an orientational phase rotated 30° [97]. It occurs an interface layer between FLG and SiC substrate due to the

covalent bonding. π states of graphene get back from the Fermi energy (E_f) and this cause to open a gap on graphene with a structure of the $6\sqrt{3}$ construction [88]. This construction layer is at the interface layer between SiC (0001) and graphene layer which occurs in the interface shows same properties with graphene.

Graphene forms much slower on Si-terminated face when compared to C-terminated face (Figure 16) [98]. With increasing annealing temperature and time, it is possible to obtain a more equilibrium form of the surface structure. According to the literature, the mobility of the electrons of graphene which is grown on Si-terminated face and under UHV conditions changes between 24-530 $cm^2V^{-1}s^{-1}$. Also, studies imply that charge carrier density of Si-face grown graphene is about 5-0.03 x 10^{-13} cm^{-2} [99].

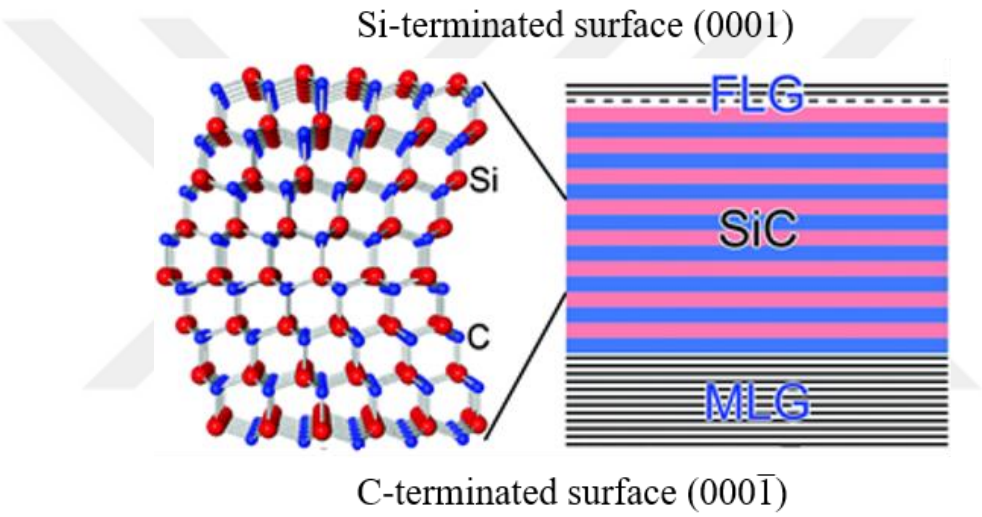

Figure 16. Illustration of layer number of epitaxial graphene on SiC on Si-terminated face (0001) and C-terminated face (000-1) [100].

2.2.2 Growth of Graphene on the C-face of SiC

Unlike growth of graphene on Si-face, during graphene formation on C-face, 2×2 and 3×3 reconstructions are observed. However, it is not expected that this reconstruction would act as a template for the graphene, so there is no coincidence between their unit cell size and that of the graphene. Compared to the Si-terminated face, there are rotationally disordered domains on C-terminated face and individual graphene layers are thicker than the layers on SiC (0001) (Figure 16). There is a strong covalent bonding between following first graphene layer and SiC (000-1) substrate while weak

interaction between graphene layers. Both misalignment and turbostratic structure of the substrate, the graphene layers are rotated on the C-face and after that other graphene layers grown with respect to each other individually [88].

In contrast to Si-terminated face, graphene forms at relatively lower temperature on C-terminated face. This difference arise from inherent energetic instability of the C-face, low energy surface. Furthermore, the rate of graphene formation on the C-face is considerably faster than Si-face. In these films, there is no Bernal stacking but rotational disordering occurs. This disorder produces a band structure which resembles to that of an isolated single layer graphene [61,81,91,93].

With epitaxial method, it is possible to obtain single and few layer graphene as mentioned in previous chapters. However; obtained graphene films on SiC (000-1) exhibit rough surfaces which are unacceptable for electronic devices. Fortunately, with capping method, it is possible to control the high sublimation rate of silicon [101], [102]. This method is used to increase the silicon vapor pressure during the annealing process. It is possible to control the number of graphene layers on the C-terminated face during the epitaxial growth. In addition to this, ARPES and transport measurements show that produced epitaxial graphene on C-terminated face has linear dispersion and high mobility (10.000-30.000 $cm^2V^{-1}s^{-1}$) [98].

CHAPTER 3

GROWTH AND CHARACTERIZATION OF EPITAXIAL GRAPHENE ON SiC

3.1. Sample Preparation

Before the growth, samples must be cleaned and well prepared. In order to be used in the growth experiments, 250 μm thick and on-axis, Si-face epi-ready, n-type 6H-SiC wafer was used. The wafer was diced into 4 x 10 mm^2 rectangular substrates. Resistivity of the samples were in the range between 0.02- 0.1Ωcm. To remove organic contaminations from the sample surface, ultrasonic cleaning was used. SiC samples were cleaned with high purity acetone (Sigma Aldrich, ≥ 99%) in ultrasonic bath for 15 min. We used acetone since it dissolves almost all the organic compounds from SiC surface. After cleaning the sample by using acetone, isopropanol (Sigma Aldrich, ≥ 99.5%) was used to remove the remaining acetone. As the last step, samples were rinsed in deionized (DI) water to remove isopropanol remains on the SiC substrate. Furthermore, the native oxide layer present on the SiC sample surface was removed by 6% diluted hydrofluoric acid (HF) solution.

3.2 Growth Set-up

All the growth experiments in this study were conducted in an ultra-high vacuum (UHV) chamber. Epitaxial graphene was grown in UHV chamber where base pressure is about 10^{-10} mbar. Epitaxial graphene growth on the SiC substrate was carried out with direct current heating method. The temperature of the sample measured by a pyrometer with ±1 ℃ resolution. In our UHV system, two different pumps were used; scroll pump and Turbo Molecular Pump (TMP). At first, for removing the contamination like small particles in the chamber, scroll pump was used which takes the system pressure down to 10^{-2} mbar. After reaching the pressure of 10^{-2} mbar, TMP is turned on to achieve a

pressure on the 10^{-10} mbar range. There are two types of vacuum gauges which are AUX1 (Cold Cathode) and IMG (Inverse Magnetron Gauge). We run AUX1 to read the pressure range between 10^{-3} mbar and 10^{-9} mbar. IMG was used to read the pressure range between 10^{-3} mbar and 10^{-10} mbar. System pressure was traced by a gauge controller. All equipment and controllers for epitaxial graphene growth system are shown in Figure 17.

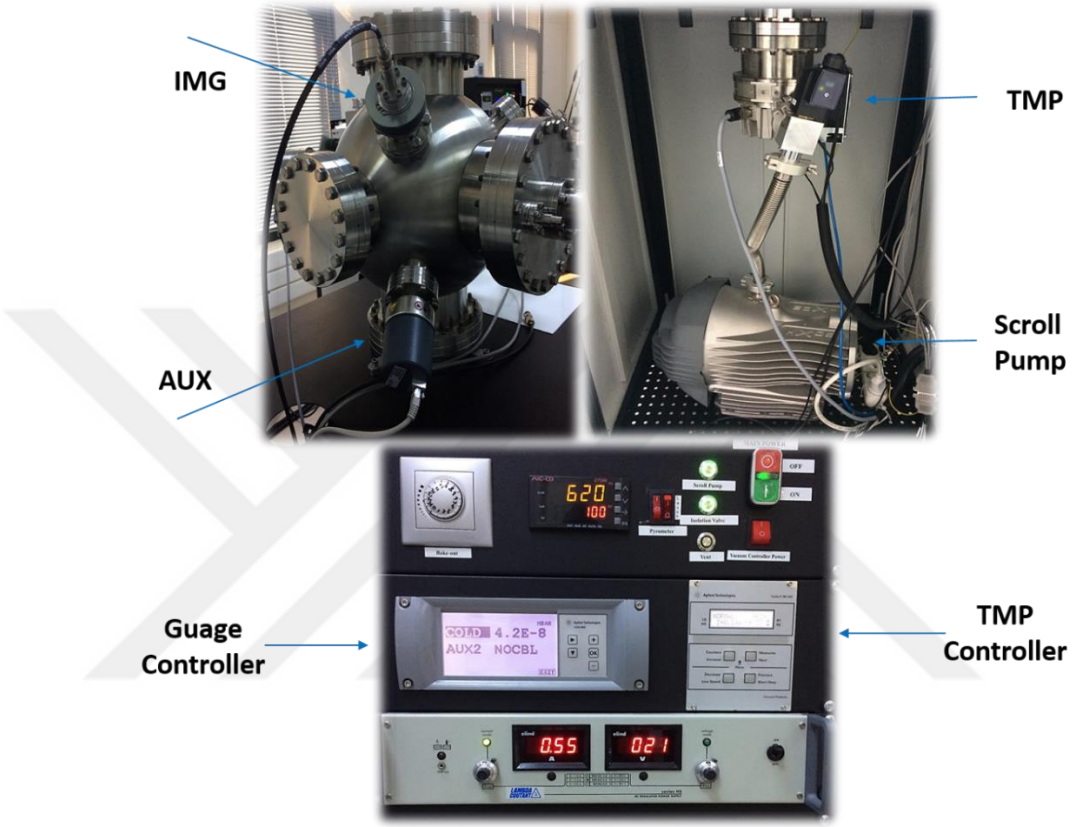

Figure 17. Epitaxial graphene growth system setup in the Department of Physics at IZTECH.

We designed a simple and user-friendly sample stage for high temperature annealing process as shown in Figure 18 (a). Sample stage was designed with special materials to resist high temperatures in due course of growth. The underside of the sample stage is Alumina Ceramic (Al_2O_3) and upside is Tantalum (Ta) (Figure 18 (b)). Both of these two materials have high melting points 2072 ℃ and 3020 ℃, respectively. In addition to resisting high temperatures, Al_2O_3 act as an excellent dielectric material which isolates Ta plates for removing any shortcut problem on the sample stage.

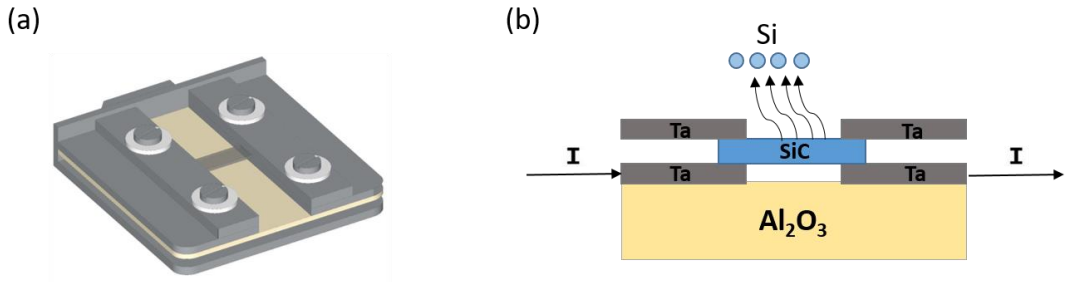

Figure 18. (a) 3D modelling of SiC annealing sample stage (b) Schematic view of the sample annealing mechanism by using direct current heating method.

3.3 Growth of Epitaxial Graphene

The growth experiment was done in three steps as seen in Figure 19. Before the graphene growth, samples were degassed at 600 ℃ overnight. This step is necessary for thermally cleaning the organics and possible contaminations from the sample surface. For removing the native oxide layer from the sample surface, substrates were heated up to about 1050 ℃ for 5 min. To enlarge the grain boundaries of the SiC substrate, temperature was increased to 1300 ℃ for 7 min. All these procedures were carried out for every sample before the growth step. Above 1350 ℃ Si atoms start to evaporate from the surface and left-behind carbon atoms form graphene structure on the SiC surface. The growth experiments were repeated as a function of temperature and time to get monolayer (1350 ℃, 3min.), few layer (1400-1450 ℃, 5-10 min.) and multilayer (1500 ℃, 20 min) graphene.

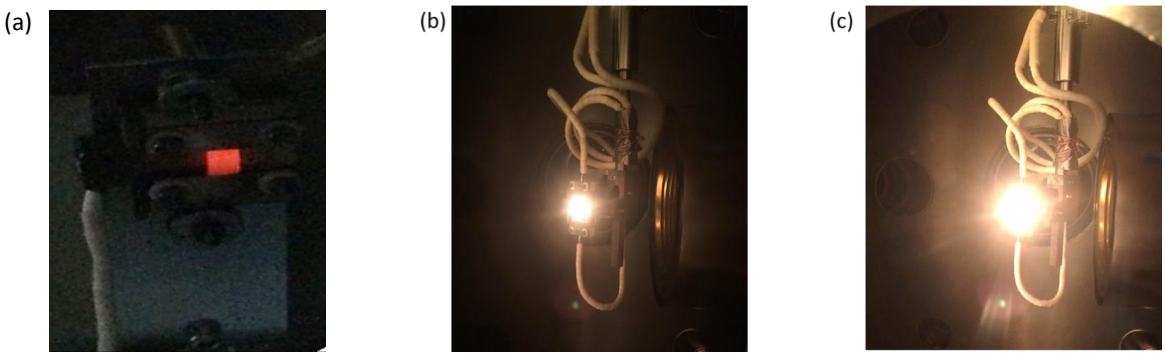

Figure 19. Epitaxial graphene growth steps with different temperatures at (a) 600 ℃ (b) 1050℃ (c) 1350℃.

In this work, the growth of graphene was done on the Si-terminated face of SiC since it is easy to control the number of layer of graphene rather than on the C-terminated face. During the growth experiments, the pressure of the chamber did not exceed ~10^{-7} mbar. By changing the growth temperature and time, different numbers of layers of homogenous graphene were obtained. Growth parameters are given in Table 1. After graphene growth, current was shut-off and the sample was allowed to cool down to room temperature.

Table 1. Epitaxial graphene growth parameters.

Sample number	Thermal Cleaning		Oxide Removal		Surface Preparation		Graphene Growth	
	T (°C)	Time (min)	T (°C)	Time (min)	T (°C)	Time (min)	T (°C)	Time (min)
EG3	600	overnight	1050-1070	10	1300-1310	7	1350	3
S1	600	overnight	1050-1070	10	1300-1310	7	1350	5
S3	600	overnight	1050-1070	10	1300-1310	7	1400	10
S4	600	overnight	1050-1070	10	1300-1310	7	1500	20
S5	600	overnight	1050-1070	10	1300-1310	7	1450	5

3.4 Characterization of Epitaxial Graphene

The characterization of epitaxial graphene was done by Raman spectroscopy and Atomic Force Microscopy (AFM). Raman spectroscopy was used for determining layer number of graphene. The morphology of annealed and bare SiC sample surface were analyzed by AFM measurements.

3.4.1 Raman Spectroscopy Measurements

Raman spectroscopy is a spectroscopic technique based on the inelastic scattering of monochromatic light from laser source. This characterization method was first observed in 1928 and used as an efficient method in material science researches since 1940s [103]. Raman spectroscopy is a basic and main technique for obtaining set of bonds

present in the substrate. In this method, basically, the frequency of photons in monochromatic light changes upon interacted with a sample. Photons of the laser light are absorbed by the sample and then reemitted. Reemitted photons frequency is shifted up or down in comparison with original monochromatic frequency, which is called the Raman effect. This shift provides valuable information about vibrational, rotational and other low frequency vibrations in materials. Raman spectroscopy method also can be applied for solid, liquid and gaseous samples.

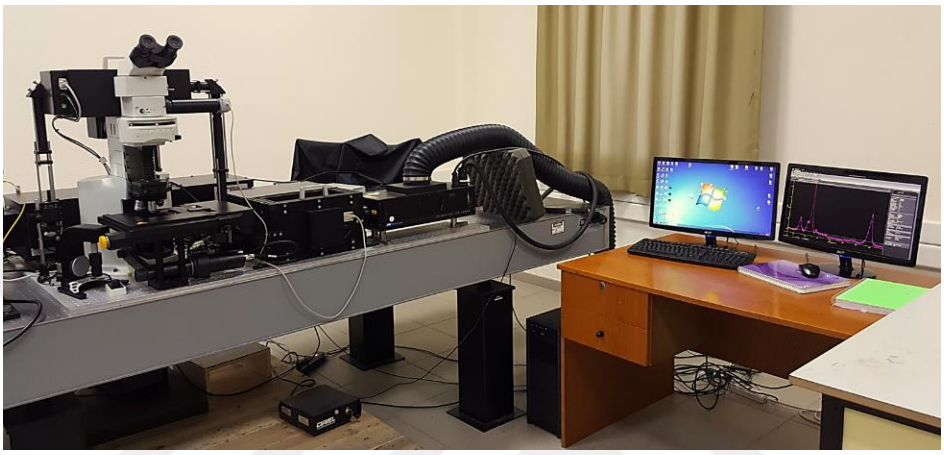

Figure 20. Raman spectroscopy measurement set-up (Monovista-Princeton instruments) in Physics Department, IZTECH.

In this thesis Raman spectroscopy was used to determine the number of graphene layer on SiC. Raman spectroscopy measurements were carried out by the Raman spectrometer in department of Physics at IZTECH as seen in Figure 20. In addition to graphene layer number determination, atomic structure of edges in graphene, defects and stacking order between different layers can also be measured [104–106]. By Raman spectroscopy, graphene has three main characteristic peaks in the Raman spectrum which are called as D, G and 2D modes. D peak appears at ~1350 cm^{-1} and is related to the disorder due to the defects in sp^2 carbon systems results in resonance Raman spectra. G band, appears at ~1583 cm^{-1} for graphene, is a first order Raman scattering process containing in-plane transverse optical and longitudinal excitations at the middle of the Brillouin zone. G peak can also be used to study the modifications of defects on graphene. Another characteristic peak for graphene is G'-peak which is found in Raman spectra at ~2700 cm^{-1}. This peak is known as the second order Raman scattering of D peak and it can be called in literature as 2D peak. The 2D peak in graphene occurs from two phonons

with opposite momentum in the highest optical branch near the K point in Brillouin zone. This peak gives information about the number of layer of graphene. However, for more than 5 layers graphene, Raman spectroscopy is insufficient to determine the difference between bulk graphite and multi layers graphene. Both G and 2D peaks give information about electron-phonon interactions in graphene. In addition to these, there is another peak at ~ 3250 cm^{-1} and this peak is the second order of the inter-valley D' peak. Its frequency is higher than double D peak but it is not its second order and this peak is called 2D'.

In this work, the Raman spectrum of our samples were measured with Monovista (Princeton Instruments) Raman system. An Ar^{+} ion laser with a 514 nm (2.41 eV) excitation source was used and all Raman signals were recorded in a spectral range between 1200-3000 cm^{-1} with a 600 grooves/mm grating. The laser spot size is approximately 2 μm and laser was focused by 100x optical lens. Each spectrum was analyzed using the TriVista software. The thickness homogeneity of the grown graphene samples was determined by micro-Raman mapping method as discussed in literature [108,109].

Epitaxial graphene was grown on Si-face surface of SiC with changing temperatures between 1350-1500℃ and annealing times between 5-20 min. The obtained Raman spectroscopy measurement results were compared with the literature for determining the number of layers and homogeneity of graphene [88].

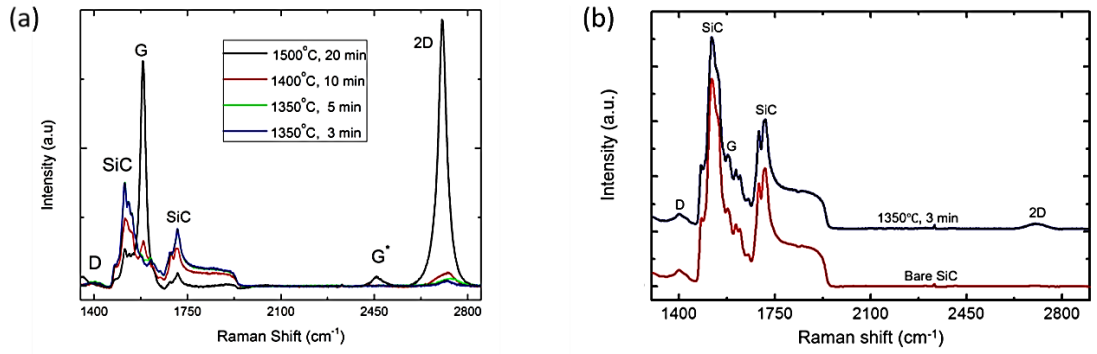

Figure 21. (a) Raman measurements on the Si-face surface of SiC substrates annealed at different temperatures and period of time. (b) Raman spectroscopy measurements of epitaxial graphene grown at 1350 ℃ in 3 min. and bare SiC.

As shown in Figure 21 (a), Raman measurements of the epitaxial graphene grown on Si-terminated SiC substrate were compared for different growth temperatures and annealing times. As mentioned previously, exfoliated and CVD graphene have three

characteristic peaks, named as D, G and 2D. However, in the Raman signal of epitaxial graphene, SiC has a dominant background peak with respect to other characteristic peaks of graphene. SiC Raman peaks appear at ~1515 cm^{-1} and ~1715 cm^{-1} respectively [109]. Both G and 2D band peak intensities do not vary with the position suggesting that the thickness of epitaxial graphene layer is uniform throughout the underlying SiC surface. The decrease in SiC signal and the increase in 2D peak intensity show that the amount of graphene layer increases with the growth time. It is clearly seen that in Figure 21 (a), when we compared with 2D peak intensities, the intensity is increasing while the number of graphene layer is increasing too. The Raman spectra of graphene grown at 1500℃ for 20 min., the SiC peaks are not visible. This is the result of the dominance of the G peak arising from the graphitic structure formed on the surface. In addition to this, G* peak is occurred also. This band is originated from a combination of the zone boundary longitudinal acoustic phonon and in-plane transverse optical phonon modes. If the number of the layer increases, a redshift in G* peak occurs [110].

The aim of this study is to obtain the appropriate growth parameters to obtain single layer of epitaxial graphene on SiC. To determine the exact number of graphene layer on SiC substrate, Raman attenuation method is carried out [111]. In this method, the SiC attenuation fraction $e^{-2\alpha t}$ is extracted by the subtraction of a scaled bare SiC substrate from the obtained Raman spectrum of epitaxial graphene on SiC substrate where t is the thickness of graphene and α is the absorption coefficient of graphene. The 2D peak intensity comparison between graphene grown at 1350 ℃ at 3 min. and bare SiC shown in Figure 21 (b). It is very common that for mechanically exfoliated monolayer graphene, I_{2D}/I_G ratio is about 2 and for higher number of graphene layers, I_{2D}/I_G ratio becomes lower[16]. After the attenuation, obtained Raman profile reveals that the characteristic G and single Lorentzian 2D peaks that are similar to those of mechanically exfoliated monolayer graphene on a 300 nm thick SiO_2 substrate Figure 22 (a). For obtaining monolayer graphene, growth time and annealing time has been found to be 1350 ℃ and 3 min., respectively.

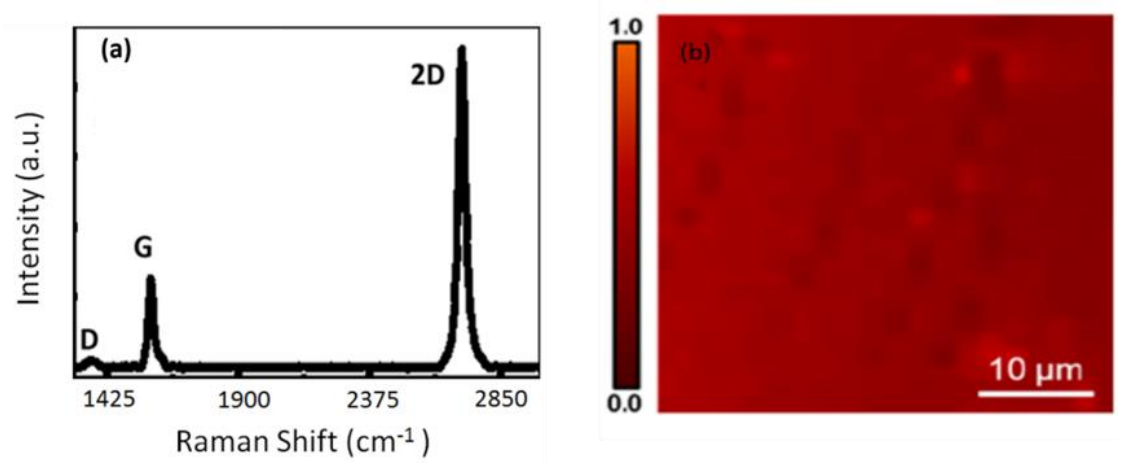

Figure 22. (a) Raman signal of epitaxial graphene after the attenuation method (b) 35 µm x 35 µm area 2D and intensity Raman map of monolayer epitaxial graphene.

In order to the determine the graphene thickness uniformity, large area micro-Raman mapping was conducted within the wavenumber range between 2500 cm^{-1} and 2900 cm^{-1} as shown in Figure 22 (b). The obtained data was recorded for 1 µm step size with a precision two dimensional stage. From the Raman map measurement, the 2D peak intensity variation σ (I_{2D}) throughout the graphene layer was calculated to be only about 4%. This small variation in the 2D peak intensity could be due to the intensity fluctuation of the excitation laser source [101].

3.4.2 Atomic Force Microscopy Measurements

Atomic force microscopy (AFM) is a very useful characterization technique to measure the surface topography of the samples down to nanometer scales. It was developed in 1986 as a combination of the Scanning Tunneling Microscopy (STM) and stylus profilometer [112]. AFM is a versatile technique since it is possible to measure not only three dimensional surface topography of the samples but also enable to study surface characteristics by the help of nanoscale sharp probe.

As depicted in Figure 23 (a), AFM is a surface characterization method which uses a cantilever with a sharp tip scan over the sample surface. The tip is supported on a flexible cantilever usually made from Si. When tip approaches close enough to the

surface, an attractive force between the sample surface and tip occurs, hence this causes the cantilever deflect towards the surface. Upon contacts this force becomes repulsive. Cantilever deflection causes small changes in the direction of reflected beam. A photo diode sense this small change and resulting cantilever deflection is recorded. By using feedback loop to control the height of the tip above from the surface and 3D image of the surface topography mapping of the sample can be obtained.

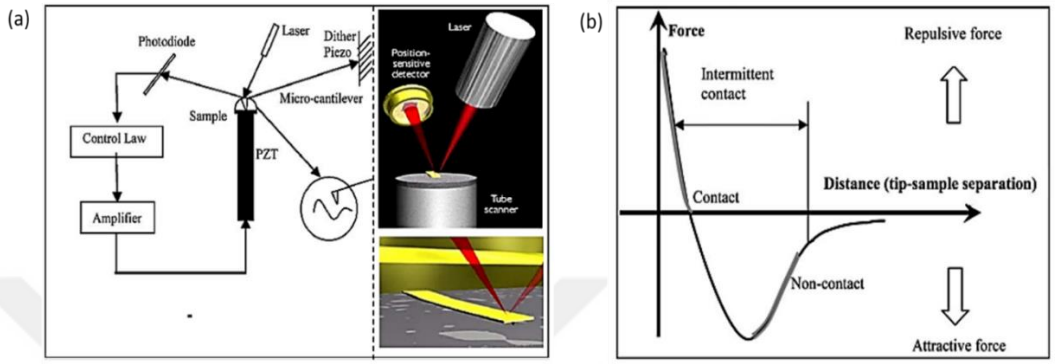

Figure 23. (a) Schematic representation of working principle and components of AFM (b) Interaction force versus distance between AFM tip and sample surface [113].

The interaction between tip and the sample is strongly dependent on van der Waals and chemical forces [114]. These interaction can be categorized into two section which can be seen in force-displacement curve in Figure 23 (b). If the interatomic distance is large, then it occurs attracted force between tip and the sample. When atoms getting closer to each other quite a bit, electron clouds repel to each other and this attractive force is decreasing in magnitude. As a result the interaction force reaches to zero and it becomes completely repulsive.

In this work, the topography of the epitaxial graphene samples were analyzed with tapping mode AFM. All the data were taken with Digital Instruments-MMSPM Nanoscope IV in the Centre of Materials Research in IZTECH. High resolution AFM images were acquired for 50 μm x 50 μm surface area.

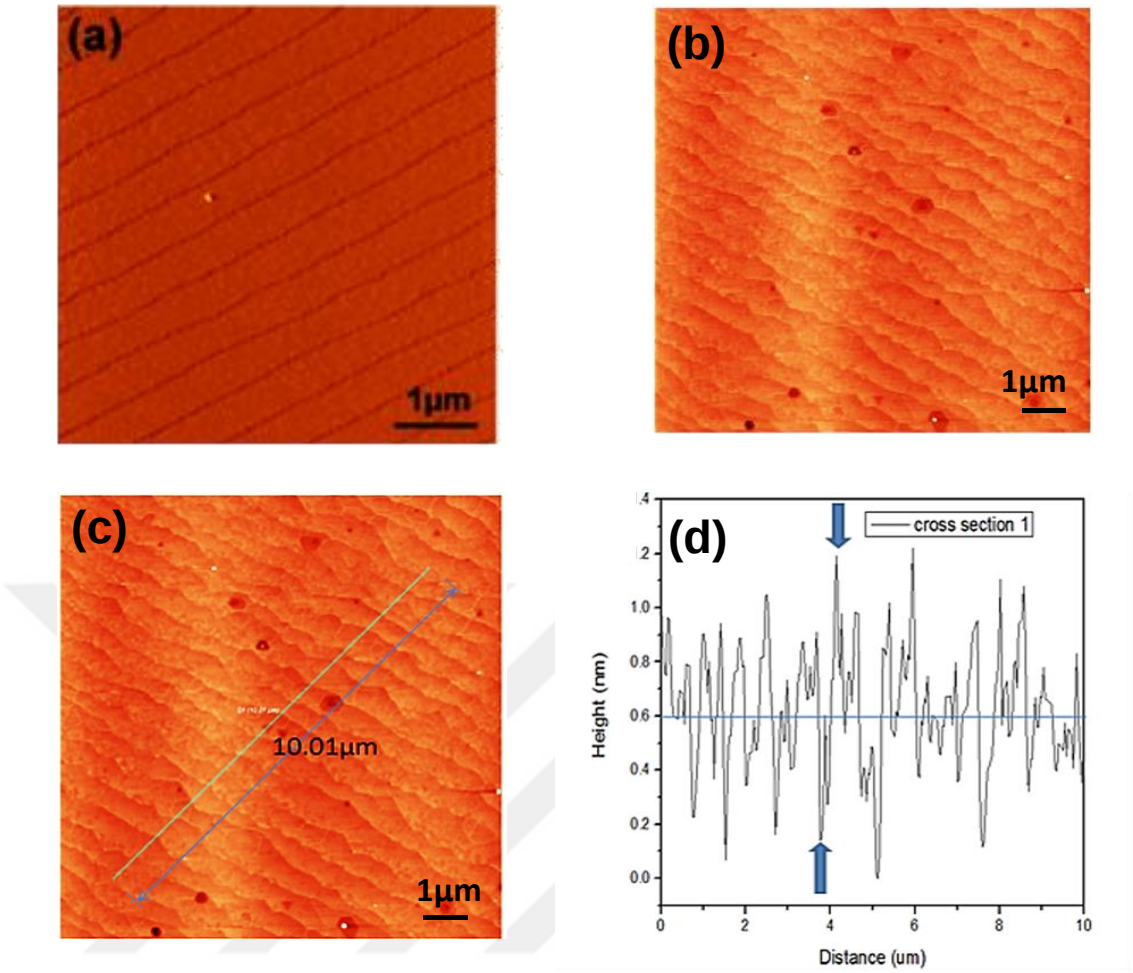

Figure 24. (a) AFM topography image of as-received SiC substrate (b) AFM topography measurement of the SiC surface after annealing process 10 µm x 10 µm area. (c) AFM cross section randomly selected area (d) AFM line profile measurement of terraces after annealing SiC.

The surface morphology of the as-received and annealed SiC substrate were analyzed by AFM measurements. The results were compared bare SiC with after annealing SiC. As-received SiC AFM measurement (Figure 24 (a)) show that sample surface was dominated with 0.5-0.6 µm wide terraces. These terraces were created during the preparation of epi-ready SiC surface. After epitaxial graphene growth, the surface morphology of the annealed SiC substrate was measured by AFM topography measurements (Figure 24 (b)). The AFM measurements obtained after the annealing process indicates 2-5 µm wide-step terraces separated by step edges with heights range depending on the width of the terraces. On the other hand, some dark spots were observed

on the SiC substrates which may arise during the annealing process. These dark regions are the nucleation centers that stimulate the graphene growth.

The height of the terraces determined by subtraction of the minimum value of the signal from the maximum value in line profiles. As shown in Figure 24 (c) and (d), the height of these terraces was measured as about 1.06 nm. Our analysis showed that, the average height of each terrace is approximately 0.6 nm.

3.5 Summary

For obtaining single layer epitaxial graphene, the growth parameters including growth temperature and time were examined. The layer number of graphene was determined by Raman spectroscopy measurements. We found that single layer graphene is grown in UHV at a temperature of 1350℃ for 3 min. annealing time. Furthermore, to determine the homogeneity of the epitaxially grown graphene, large area (35 μm x 35μm) single point Raman mapping were performed. According to the measurement, there was a small variation in the 2D peak intensity which is 4%. The obtained results show that grown graphene with epitaxial method has uniform thickness.

AFM measurements were performed to determine the surface morphology of the grown graphene layers and as well as bare SiC substrate. After annealing process, surface morphology was changed with as-received SiC as well as after epitaxial growth graphene on SiC substrate. The height of the terraces were determined about 1.06 nm and also average height of the each terrace were measured about 0.6 nm.

CHAPTER 4

FORMATION OF SiO_2 WRINKLES ON EPITAXIAL GRAPHENE

4.1 Thermal Evaporation System

Thermal evaporation system is one of the basic Physical Vapor Deposition (PVD) technique. This technique is operated based on heating of the target material in a vacuum chamber (P ~ 10^{-7} mbar) until its surface atoms have sufficient energy to leave from the surface. The evaporated material constitutes a vapor stream, which traverses the chamber and hits the substrate, sticking to it as a thin film.

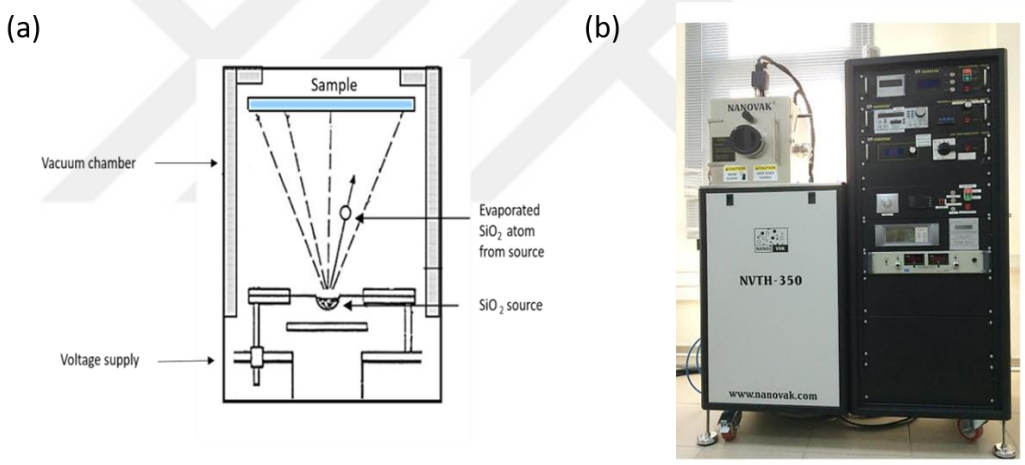

Figure 25. (a) Schematic representation of thermal evaporation system (b) Thermal Evaporation system (Nanovak NVTH-350) at the Department of Physics in IZTECH.

Thermal evaporation system and their equipment were shown in Figure 25 (a). Our thermal evaporation system (NANOVAK NVTH-350) is equipped by four sources to evaporate four different materials such as chromium (Cr), nickel (Ni), gold (Au) and silicon dioxide (SiO_2) (Figure 25 (b)). In this system, it is possible to anneal the sample under vacuum conditions and the annealing temperature can be read with a thermocouple ($\pm$1℃ resolution). The base pressure of the system is about 4×10^{-7} mbar that is

achieved by using mechanical and turbo pumps. The film thickness is measured by two quartz crystal microbalance sensors which are placed at the same height as the sample holder.

4.2 SiO_2 Thin Film Deposition on Bare SiC and on Epitaxial Graphene

After the growth of monolayer epitaxial graphene, 15 nm thick SiO_2 film was deposited onto a set of bare SiC and epitaxial graphene substrates by the thermal evaporation system mentioned previously. For the evaporation of SiO_2, tungsten (W) basket was used. The boat was connected to the electrodes placed in a vacuum chamber. There is a shutter between boat and the sample. With the shutter closed, a voltage was applied to the boat in order to heat it which was determined by a relation between the deposition rate of SiO_2 in vacuum and applied voltage. For the deposition, current and power was set to 40 A and 217 W, respectively. The tungsten boat was heated and SiO_2 was evaporated in vacuum ambient. SiO_2 film were formed on a substrate after the shutter was open [115]. During the SiO_2 thin film deposition process, the sample temperature was measured as 60℃. After the deposition stage the sample was cooled down to room temperature (~27℃ in our case) inside the vacuum chamber and then was taken to the ambient. The surface morphology of the samples were characterized by Optical Microscopy (OM) and Scanning Electron Microscopy (SEM) measurements as shown in Figure 26 (a), (b) and Figure 26 (c), (d), respectively.

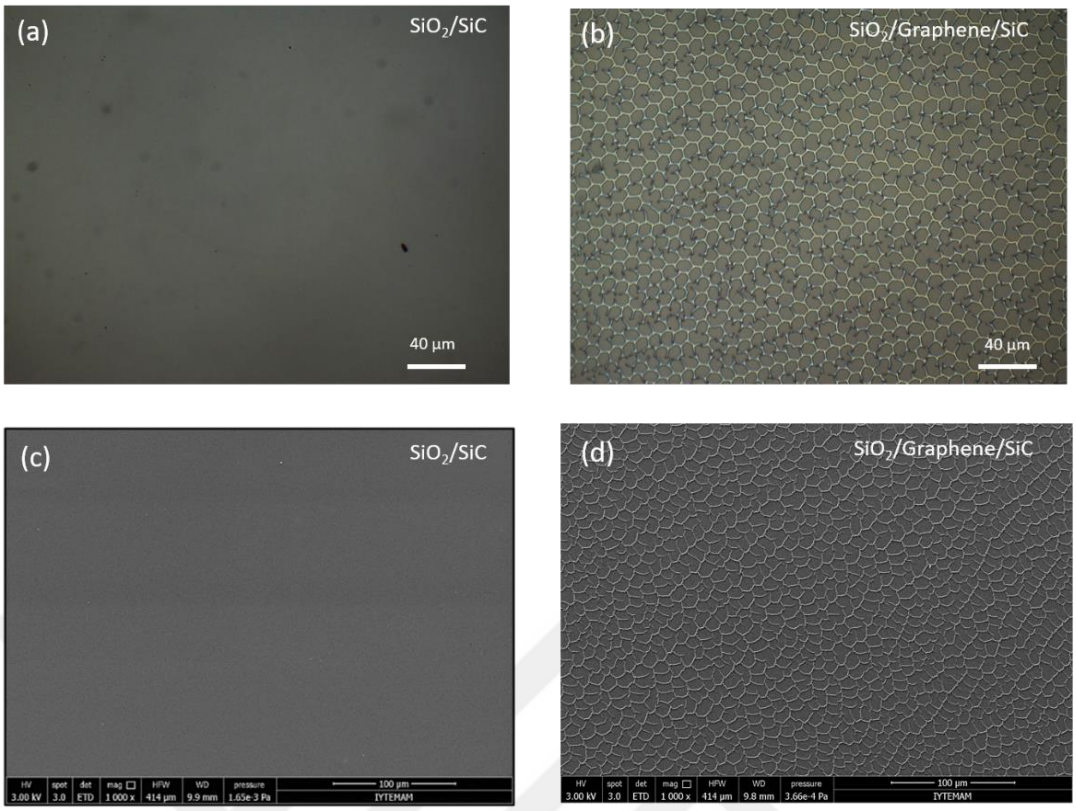

Figure 26. Optical microscope image of 15 nm thick SiO_2 thin film deposited onto (a) bare 6H-SiC substrate and (b) monolayer epitaxial graphene. High-magnification SEM image of 15 nm thick SiO_2 thin film deposited onto (c) and bare 6H-SiC substrate (d) monolayer epitaxial graphene.

The measurements showed that different from the one deposited on bare SiC, the SiO_2 film on epitaxial graphene exhibits a self-assembled network of hexagonally shaped wrinkle structures (Figure 26 (b) and Figure 26 (d)). For T = 60 ℃ deposition temperature (or substrate temperature) and 15 nm thick SiO_2 thin film, the mesh size of the wrinkle network was found to range between 15 and 20 μm and the average wrinkle to wrinkle distance measured along different surface orientations was determined as ~13 μm. The wrinkle structures spread uniformly over the entire surface area and remain stable in ambient conditions.

The common occurrence of a mesh-like network of ridges in monolayer graphene grown at elevated temperatures suggests that wrinkle formation is related to thermal-induced buckling of monolayer graphene due to negative thermal expansion coefficient ($\alpha_{graphene} = -8 \times 10^{-6} K^{-1}$) epitaxial graphene. Considering the TEC and Young's modulus values of SiO_2 ($\alpha_{SiO_2} = 0.5 \times 10^{-6} K^{-1}$, $E_{SiO_2} \approx 70$ GPa) [116] and of single crystal SiC (α_{SiC}

$= 4.1 \times 10^{-6} K^{-1}$, $E_{SiC} \approx 700$ GPa) [18], the magnitude of strain for the SiO_2 film on bare SiC surface should be much greater than that of SiO_2 layer on epitaxial graphene for the same deposition parameters. Hence, similar to the case of SiO_2 layer on epitaxial graphene, the wrinkle formation should definitely be expected also for the SiO_2/SiC samples. Moreover, the onset of wrinkling cannot be explained only in terms of the magnitude of thermal strain itself. It is known that the compressively strained films with low adhesion on compliant substrates have a great tendency to buckle and delaminate as a result of the strain relaxation [117,118]. Unlike for the SiO_2/SiC samples, where SiO_2 thin film is supposed to be strongly adhered to the SiC surface, SiO_2 is weakly attached to the epitaxial graphene layer only via van der Waals forces. Consequently, the SiO_2 thin layer tends to shrink more readily on epitaxial graphene than on bare SiC surface to form wrinkles upon cooling from the deposition temperature. This process can be intimately associated with both the viscous flow of the amorphous SiO_2 thin film and the friction characteristics of the epitaxial graphene layer.

4.3 Characterization of SiO_2 Wrinkle Structures on Epitaxial Graphene

The morphology and the structural properties of the observed SiO_2 based wrinkle structures formed on epitaxial graphene were studied by using OM, high magnification SEM and AFM measurements. As can be seen in the optical microscope images (Figure 27 (a) and Figure 27 (b)) the observed wrinkle pattern reflects the hexagonal symmetry of underlying epitaxial graphene template but with larger mesh sizes that do not correspond to the typical grain size of epitaxial graphene on SiC [119,120].

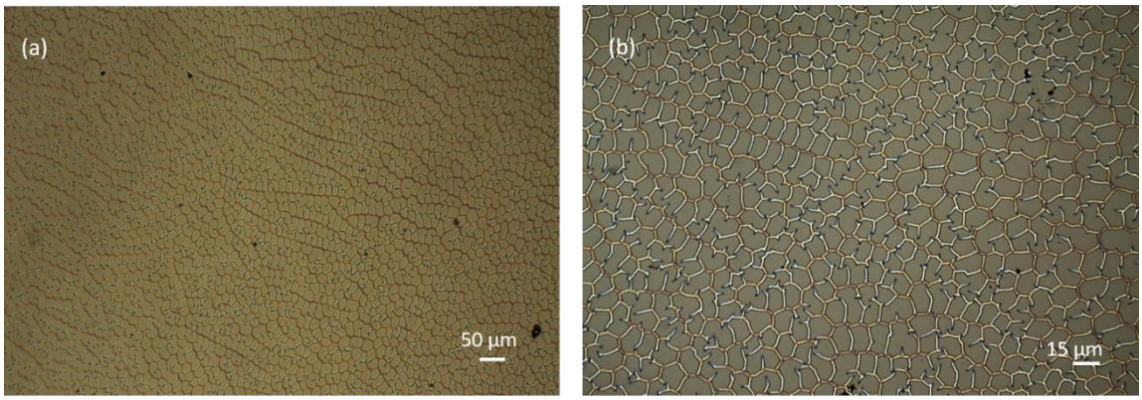

Figure 27. Optical microscope image of hexagonal wrinkle network after deposition of 15 nm thick SiO_2 thin film on monolayer epitaxial graphene with (a) 20X and (b) 50X magnification.

High magnification SEM measurements showed that the wrinkles exhibit a separation into two characteristics parallel strands. Three of these stranded wrinkles sharply fold and intersect and the coalescence of these stranded wrinkles give rise to individual nodes (Figure 28). The angle between the two wrinkles was measured as $118\pm5°$ suggesting the hexagonal lattice characteristics of the wrinkle pattern. SEM measurements implied that the wrinkle network comprise mainly wide and narrow branches. The topographic characteristics of these observed branches and the node regions were investigated in detail by AFM measurements which shown in Figure 29.

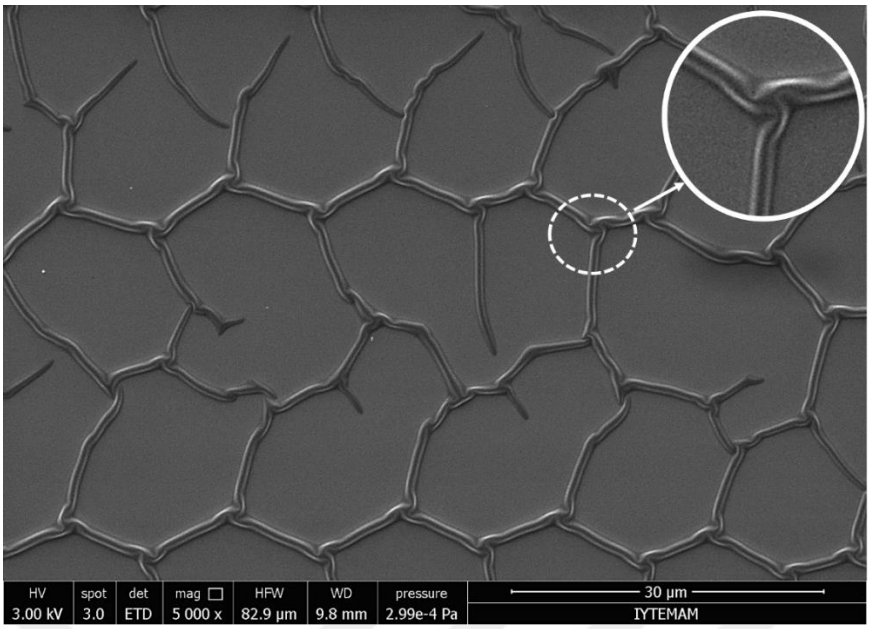

Figure 28. High-magnification SEM image of the SiO_2 wrinkle structures and their coalescence forming individual nodes on monolayer epitaxial graphene.

The SiO_2 wrinkle network was characterized also by AFM operated in the tapping mode. The linear protrusions seen in the AFM topography image (Figure 29 (a)) were classified as primary and secondary wrinkles depending on their morphology and height profiles. The distinction between a primary wrinkle and a secondary wrinkle can be explained as in the following manner: (i) unlike the secondary wrinkles, the primary wrinkles propagate along a zigzag path and do not intersect with each other to create wrinkle nodes; (ii) the maximum height of a secondary wrinkle is typically lower than that of a primary wrinkle and (iii) the height of a secondary wrinkle gradually decreases as it penetrates into a flat facet, whereas a primary wrinkle reveals a reasonably uniform height and width in between the two individual nodes. Three-dimensional (3D) topographic AFM measurements of hexagonal SiO_2 wrinkle network was shown in Figure 29 (b).

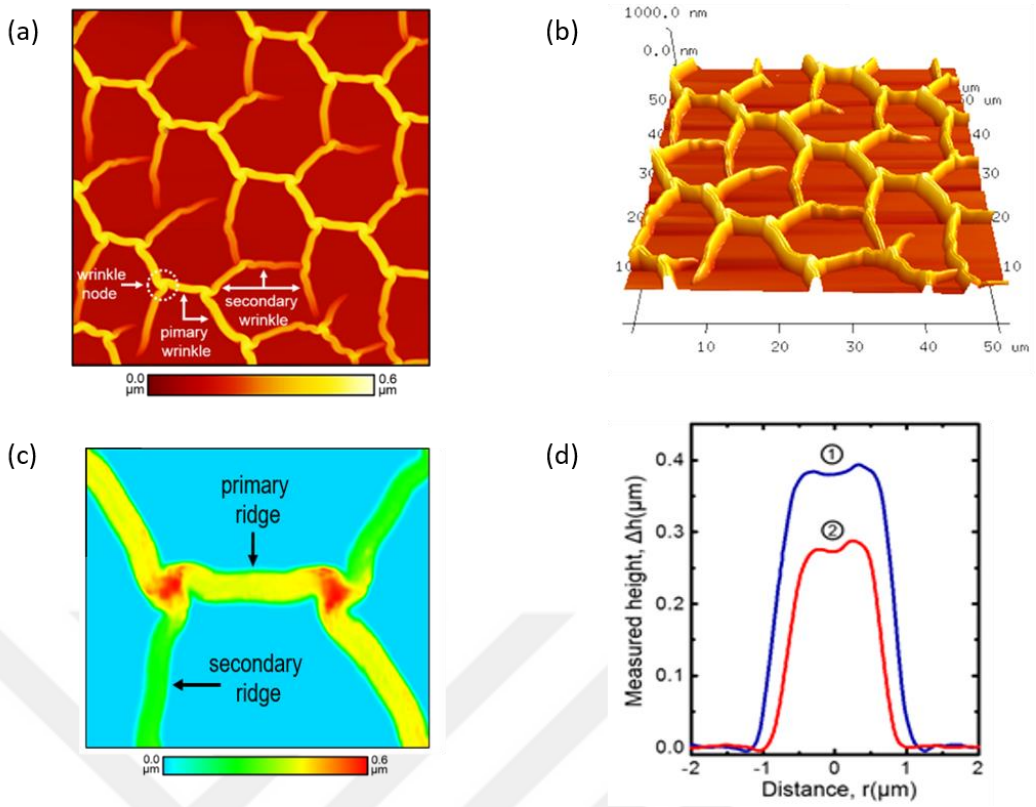

Figure 29. (a) 50 x 50 µm^2 AFM topography image of SiO_2 wrinkle network created on monolayer epitaxial graphene. (b) Three dimensional (3D) AFM topography image of SiO_2 wrinkle network on monolayer epitaxial graphene. (c) 12 x 12 µm^2 AFM topography image of primary and secondary wrinkles forming the individual wrinkle nodes with localized height protrusions. (d) Cross-sectional line profiles of primary and secondary wrinkles acquired along the arrows marked with 1 and 2 in (c).

A number of cross-sectional line profile measurements manifest that the average height and the width of a primary wrinkle is about 0.38 µm and 2.4 µm, respectively. As displayed in the high magnification AFM image (Figure 29 (c)), the intersection of the wrinkles gives rise to about 0.5 - 0.6 µm high localized hillocks in the node regions. The asymmetric protrusions appearing at the apex of the line profiles, as shown in Figure 29 (d) correspond to the two characteristic parallel strands similar to these observed in the SEM measurements (Figure 28). It has been shown that when the magnitude of compressive strain exceeds a critical value, which is usually much larger than the one required for the onset of wrinkling, similar modes of surface instabilities (e.g., coexisting folds or period doubles) are more likely to occur but in soft thin film/substrate bilayer structures [121].

In order to determine if these observed protrusions are hollow or not, the sample was immersed into 1% diluted HF solution. The sample was etched for different times such as 3, 6 and 9 seconds and then was rinsed in deionized water at least three times for removing HF residues from the sample surface. Thereafter, the sample was dried gently with nitrogen gas. The HF etching experiments showed that for 9 sec. etching time the wrinkle structure were completely removed. The surface topography of the sample and its corresponding height profiles were determined by AFM measurements. The results of AFM topography measurements obtained for 3, 6 and 9 sec. etching times were compared to the one for non-etched sample. The obtained results are shown in Figure 30.

We found that the average height of the wrinkles first increase from 424.5 nm (before etching) to 503 nm (for t = 3 sec. etching time). However, the average height decreases to 416.8 nm (for t = 6 sec. etching time). The increment of wrinkle average height in the first 3 sec. is due to the reduction of SiO_2 film thickness. It is known that the compressive strain acting on a thin film greatly increases by the reduction of thin film thickness [12,66]. As the magnitude of the strain is increased, this will promote the outward relaxation of the thin film further, hence the average height of wrinkles is increased as well. On the other hand, for further etching times such as 6 sec. the amount of SiO_2 in the regions between wrinkles is reduced so that the deformations are more likely to occur in these regions. This causes a significant lateral relaxation of the wrinkles instead of vertical outward relaxation. As a consequence of this effect, a reduction in the average wrinkle height is observed. Our experiments explicitly showed that there is an interplay between the thin film thickness and the amount of material that constructs the thin film itself. We know from the literature that the etch rate of 1% HF at room temperature is about 0.05 nm/sec. This etch rate of HF is not sufficient enough to completely remove the SiO_2 based wrinkles with a wall thickness of 15 nm in 9 sec. Even if we assume that the wrinkles are completely filled by its constitute SiO_2 material it should take at least 450 sec. to completely etch away the wrinkle structures. However, the AFM measurements show that the wrinkles are completely disappeared within a time period of 9 sec. (Figure 30 (d)). This result implies that the wrinkles are hollow.

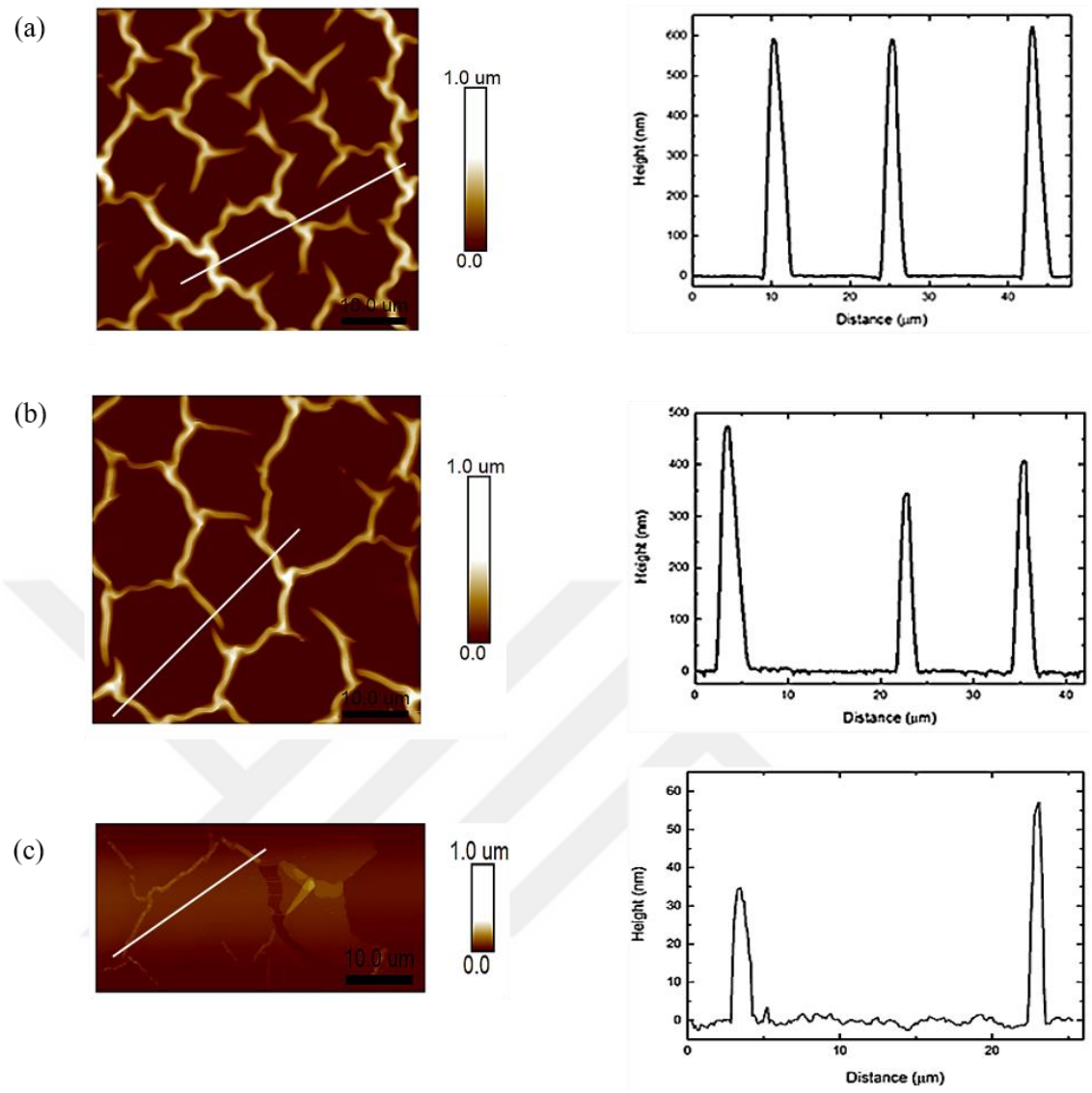

Figure 30. 50 x 50 μm^2 area 2D topographic image and height profile of 15 nm SiO_2 thin on SiC (a) after 3 sec. HF etching (b) after 6 sec. HF etching (c) after 9 sec. HF etching.

Table 2. Calculated average height and width measurements of SiO_2 wrinkles before and after HF etching process for different time intervals.

Time (sec.)	Average Height (nm)	Average Width (μm)
0	424.5	2.97
3	503	3.16
6	416.8	3.1
9	-	-

4.4 The Dynamics of SiO_2 Wrinkle Formation on Epitaxial Graphene

The dynamics of the wrinkle formation was investigated using an optical microscope immediately after the SiO_2 thin film deposition process and the measurement data were recorded in real time by a CCD camera. The snapshots taken at 120 sec. intervals reveal the surface propagation and spontaneous branching/networking of the wrinkle structures (Figure 31). The optical microscope image at t = 0 sec. (Figure 31 (a)) corresponds to the initial stage of the measurement recording process. The partial network seen in Figure 31 (a) imply that the wrinkle formation has already been initiated randomly on different regions of the sample surface till the beginning of optical microscope measurements. After t = 120 sec. wrinkle structure continued to form as a network as shown in Figure 31 (b). Until t = 240 sec. the imaged spot of the surface has been covered in a large extent by the wrinkle pattern Figure 31 (c). Further measurements showed that only a few more wrinkles are formed and linked up with the existing network within several minutes after t = 240 sec. From these time dependent optical microscope measurements, the average velocity of wrinkle propagation was determined to be greater than 1 μm/s. As represented in Figure 31 (d) this relatively fast dynamics indicates that the wrinkling can be associated with the sudden relaxation of the SiO_2 thin film on epitaxial graphene layer due to the compressive strain.

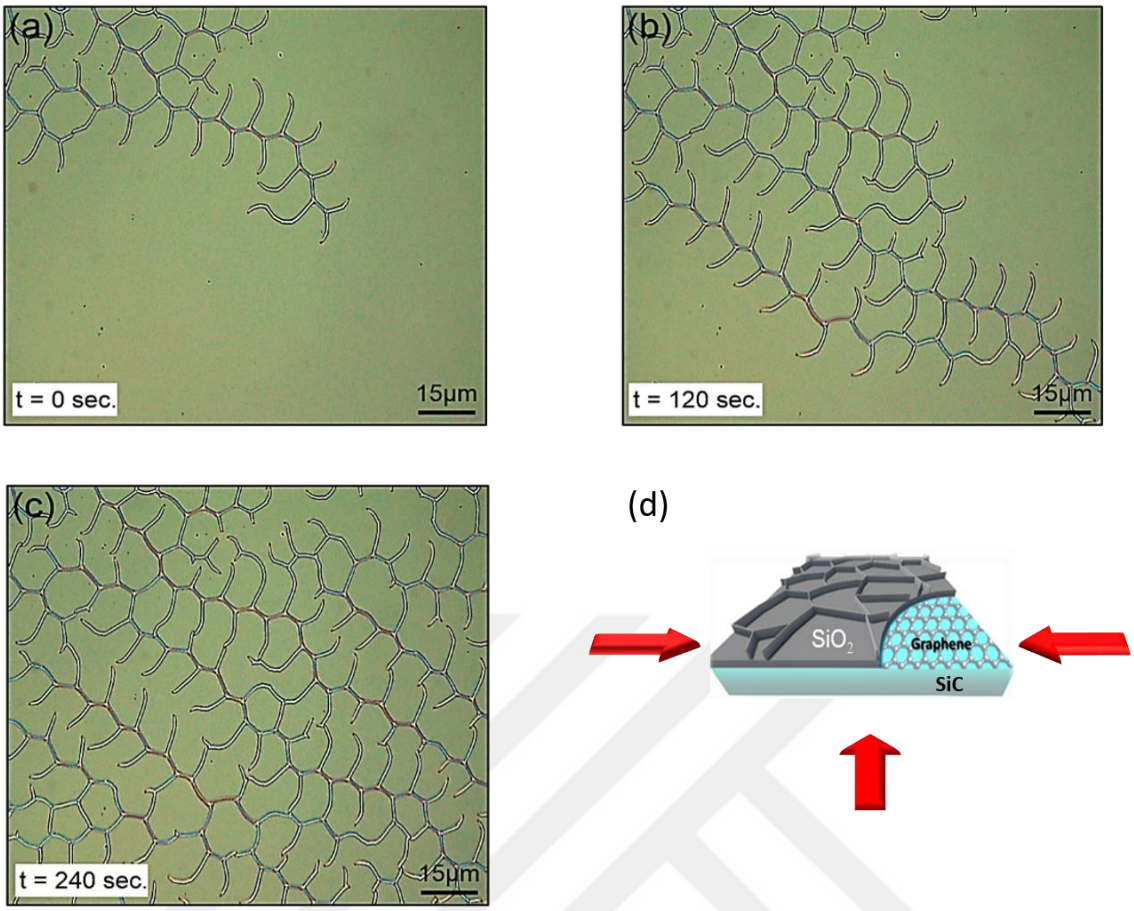

Figure 31. Optical microscope images of the spontaneous formation and networking of the self-assembled SiO_2 wrinkle structures on monolayer epitaxial graphene acquired at (a) t = 0 sec. (b) t = 120 sec. (c) t = 240 sec. (d) Schematic representation of formation of wrinkles after deposition of SiO_2 thin film due to biaxial compressive strain.

4.5 Effect of Temperature on Wrinkle Formation

To systematically investigate the effect of strain on the wrinkle network morphology, SiO_2 was deposited separately on a set of epitaxial graphene templates at different temperatures ranging between 60 °C and 150 °C. Each of the samples was cooled down from the respective deposition temperature (T_d) to room temperature (T_r) in order to introduce different amounts of compressive strain on the SiO_2 thin film due to the thermal differantial $\Delta T = (T_d - T_r)$. In Figure 32 and Figure 33, typical optical microscope and SEM image of the SiO_2 thin film deposited at 60 °C was compared with the one of deposited at 90 °C and 150 °C. The magnitude of compressive strain acting on the SiO_2 film was calculated to be increased by a factor of about 2 when T_d is raised from

60 °C to 90 °C (Table 3). We found that such an increment of the strain already decreases the average wrinkle to wrinkle distance along all the surface orientations and leads to a substantial refinement in the wrinkle mesh density. For example, the mesh density of the samples deposited at T_d = 90 °C was determined to be about an order of magnitude higher than the mesh density of the samples deposited at T_d = 60 °C which is ~10^{11} cm^{-2} (Figure 34). The evolution of the average wrinkle spacing was measured as a function of T_d and the obtained results were plotted in Figure 35. We found that the wrinkle spacing decreases rapidly for lower thermal differentials and tends to saturate as T_d is raised up to 150 °C. These experimental results can be explained consistently within the theoretical model [122]. According to this model, the dominant wavelength (λ) of the wrinkling instability for a thin film subject to a compressive strain (equation 1.10) is written as

$$\lambda = \pi h_f / \left[\alpha_f \Delta T (1 - \nu_f^2)\right]^{1/2} \tag{4.1}$$

where h_f and ν_f are the thickness and the Poisson's ratio of the thin film, respectively. Considering this relation, the λ of 15 nm thick SiO_2 film was calculated for different temperatures ranging between 50 °C to 160 °C. Except for higher T_d values, the best fit to the experimentally obtained average wrinkle spacing was achieved by the SiO_2 thin film parameters of $\alpha = 5 \times 10^{-7} K^{-1}$ and $\nu = 0.24$ [123,124]. The deviation of the calculated λ, from the corresponding experimental data, at high T_d values can be explicitly attributed to the temperature dependent increase of α_{SiO_2}. It has been shown that α_{SiO_2} increases with temperature [116]. Because of this fact the theoretically calculated wrinkle spacing and hence the corresponding density slightly deviates from our experimental data obtained for high deposition temperatures.

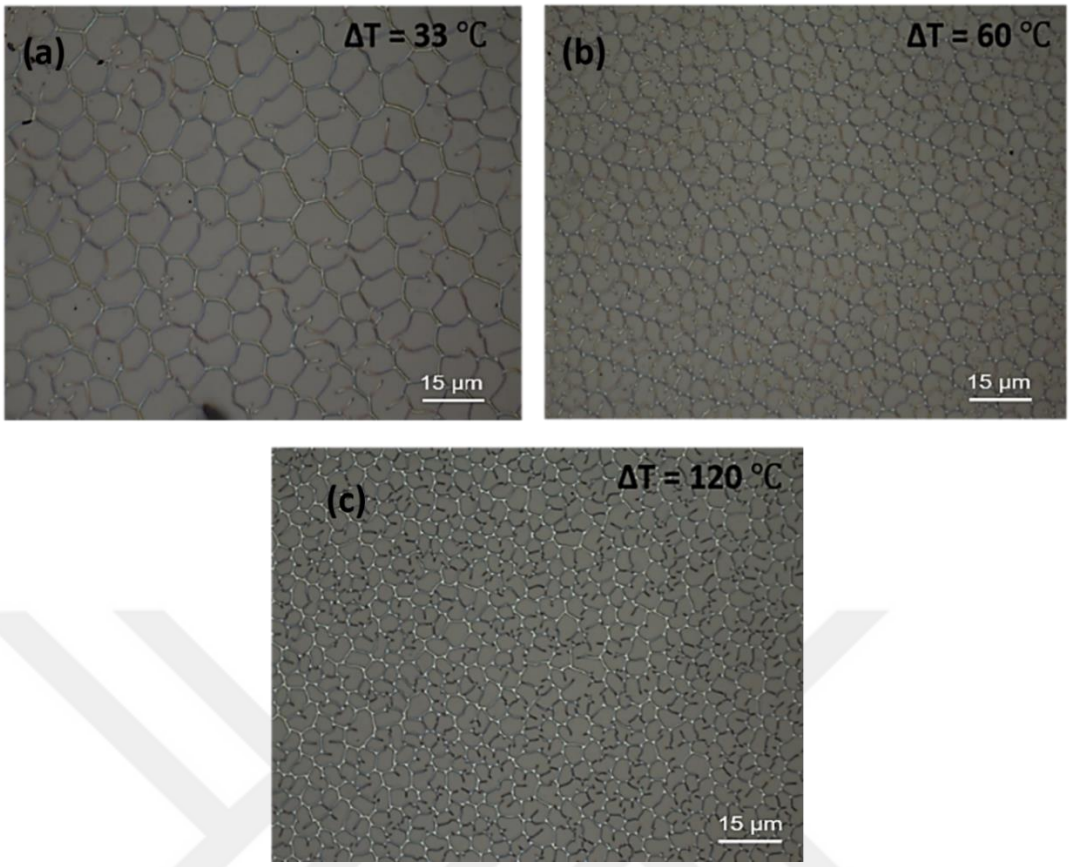

Figure 32. Optical microscope images of 15 nm thick SiO_2 thin film deposition on monolayer graphene on SiC with different temperature differentials (a) ΔT = 33 ℃ (b) ΔT = 60 ℃ and (c) ΔT = 120 ℃.

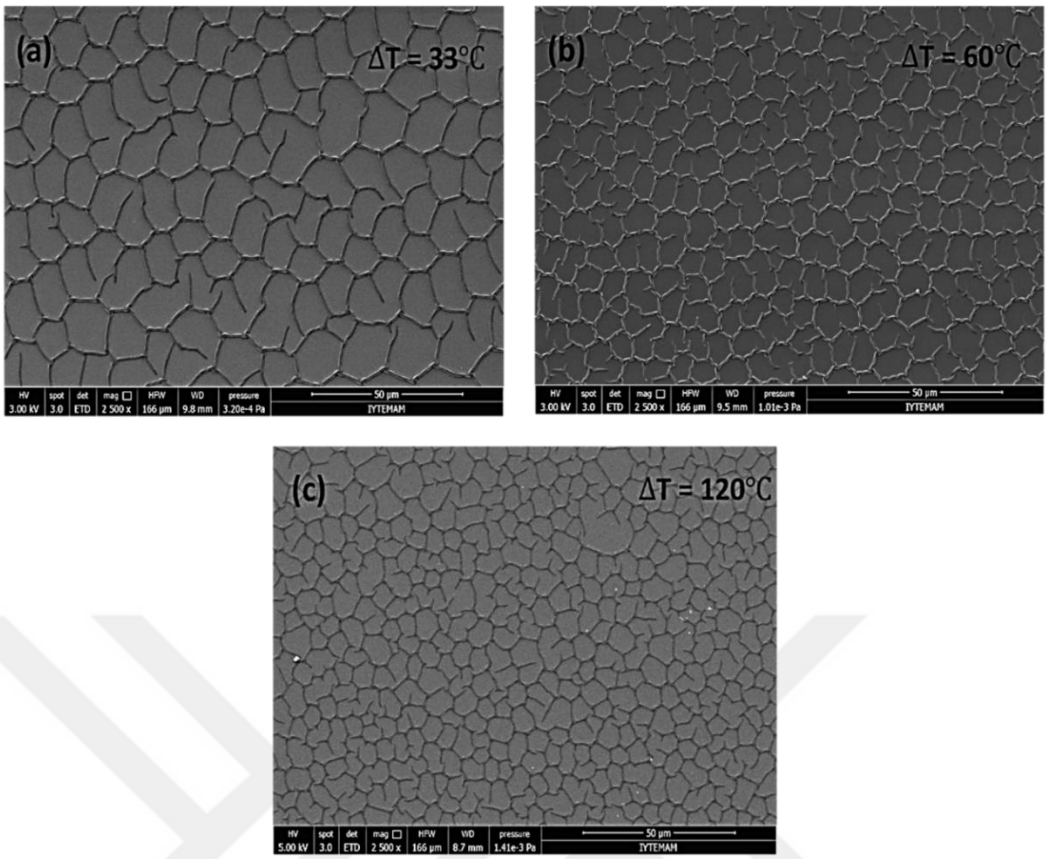

Figure 33. SEM measurements of 15 nm thick SiO_2 thin film deposition on monolayer graphene on SiC with different temperature differentials (a) ΔT = 33 ℃ (b) ΔT = 60 ℃ and (c) ΔT = 120 ℃.

Table 3. Calculated strain and wrinkle spacing with respect to deposition temperatures and temperature differential corresponding to these values.

Deposition Temperature T_d (°C)	**Temperature Differential ΔT (°C)**	**Strain σ (MPA)**	**Wrinkle Spacing λ (μm)**
60	33	1.63	12.02
90	60	2.97	8.70
120	90	4.45	7.16
150	120	5.94	6.23

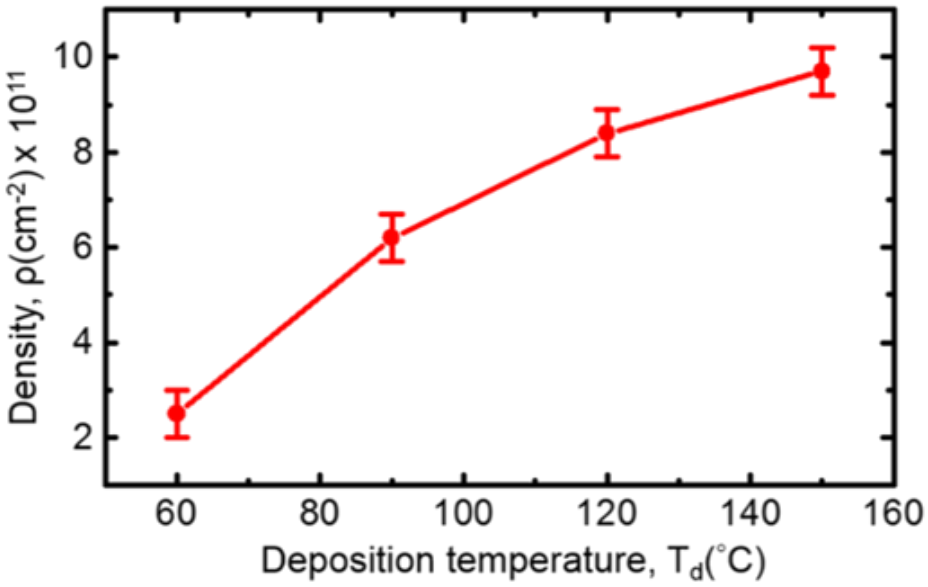

Figure 34. Experimentally obtained average wrinkle density as a function of the SiO_2 deposition temperature.

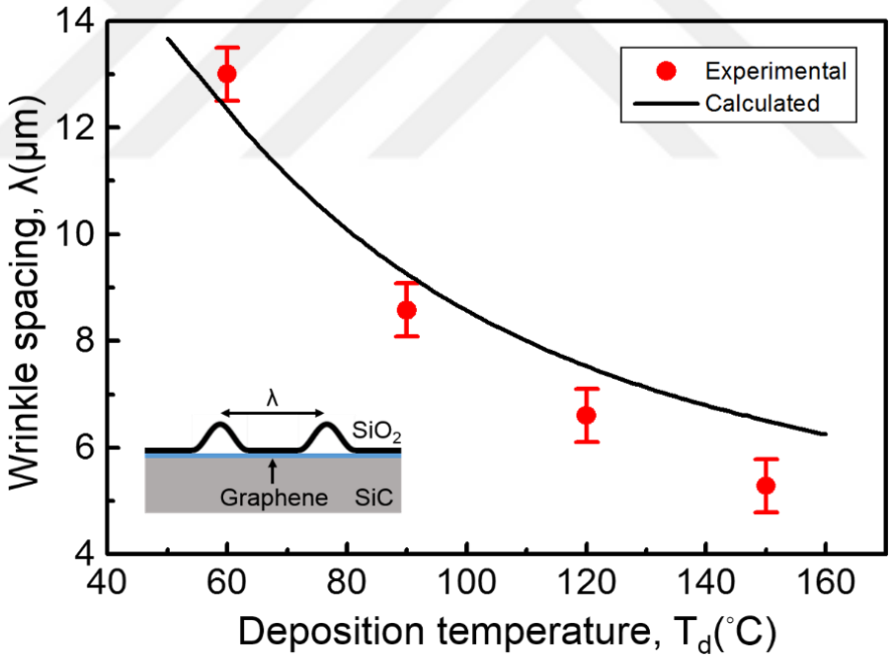

Figure 35. Experimentally obtained average wrinkle spacing as a function of the SiO_2 deposition temperature. The error bars represent the standard deviation from the corresponding average wrinkle spacing data. The solid line is the theoretically calculated wrinkling wavelength for a 15 nm thick SiO_2 film that changes as a function of temperature.

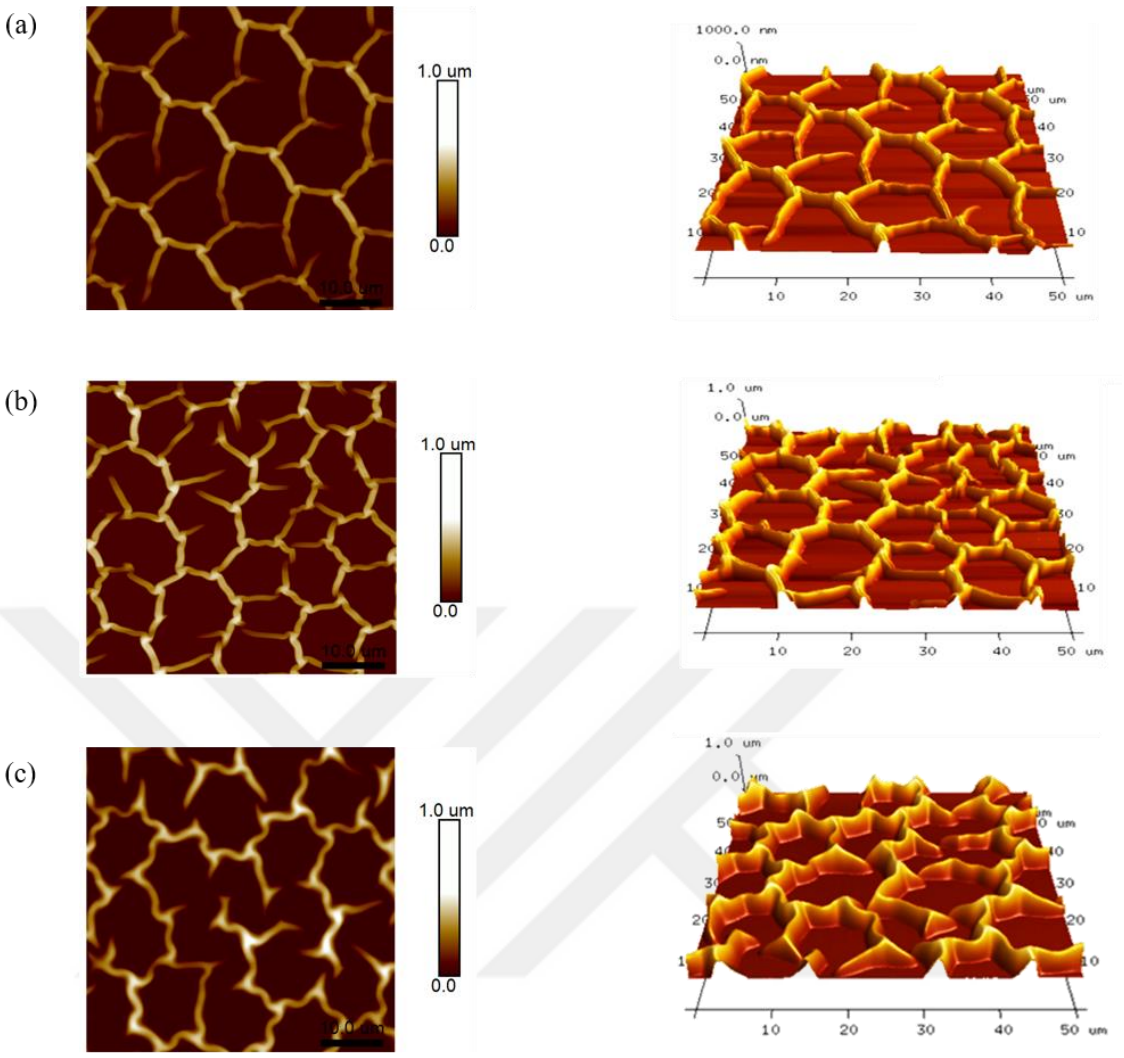

Figure 36. 2D and 3D AFM topography image of hexagonally shaped wrinkles on monolayer graphene after 15 nm thick SiO_2 thin film deposition with deposition temperature (a) T_d = 60 ℃ (b) T_d = 90 ℃ and (c) T_d = 150 ℃.

The topography of the SiO_2 wrinkle structures on epitaxial graphene was characterized in detail by AFM operated in tapping mode. To observe the effect of temperature on acting compressive strain to the surface, SiO_2 thin film deposited on monolayer graphene with different deposition temperatures. After deposition of the thin film, 2D and 3D surface topography images was investigated to see the difference in height and in the width of protrusions with deposition temperature ranging between 60 ℃ and 150 ℃ (Figure 36). The average height, width and corresponding aspect ratio (height / width) of the primary wrinkles were measured from AFM images (Table 4). As shown in Figure 36, both 2D and 3D images, the increment of the SiO_2 thin film deposition temperature on monolayer graphene, causes increase the compressive strain acting on the sample surface. As mentioned in equation 1.10, compressive strain on thin film surface is directly related to temperature differential (ΔT). The increment of ΔT, the height of primary wrinkles increase also. On the other hand, there is no dramatic change in the width of these structures.

Table 4. Measured and calculated average height, width and the aspect ratio of the wrinkles formed on monolayer graphene for different thin film deposition temperatures and temperature differential corresponding to these values.

Deposition Temperature (T_d) ℃	**Temperature Differential (ΔT) ℃**	**Average Primary Wrinkle Height ($H_{primary}$) nm**	**Average Primary Wrinkle Widht ($W_{primary}$) µm**	**Primary Wrinkles Aspect ratio (β)**
60	33	386.2	2.4	0.16
90	60	463.4	2.4	0.19
150	120	510.5	1.7	0.21

4.6 SiO_2 Thin Film on CVD Graphene

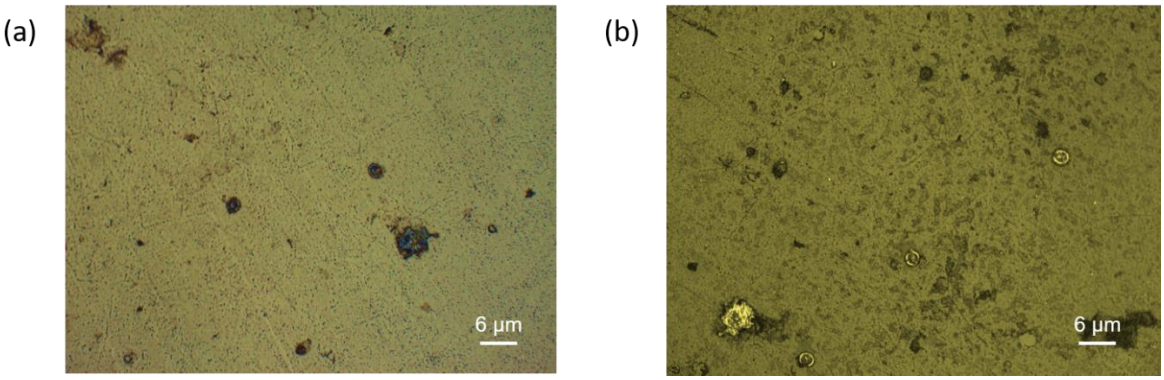

Figure 37. Optical microscope image of CVD graphene (a) without deposition SiO_2 thin film (b) after deposition of 15 nm SiO_2 thin film.

The formation of hexagonal shaped wrinkle structures were also studied on monolayer graphene grown by CVD. In order to observe wrinkle structure on the surface, 15 nm thick SiO_2 thin film was deposited on CVD graphene after transferring onto Si/SiO_2 (300 nm) substrate. Monolayer CVD graphene was grown on copper (Cu) foil at growth temperature of 1050 ℃. Growth procedure was executed at low pressure (~ 10^{-3} torr) and as a carbon precursor CH_4 (10 sccm) was used. Before the transferring process, PMMA (Poly methyl methacrylate) as a supporting layer was covered on graphene/Cu substrate by using spin coater to minimize defects on graphene during transfer process. As-grown of graphene on Cu foil was transferred onto 4 mm x 10 mm rectangular Si/SiO_2 substrate. After transfer onto Si/SiO_2 substrate, PMMA was removed from the surface with hot acetone bath. However, there are lots of studies that PMMA is not removed completely from the surface [59]. The optical microscopy image of transferred graphene on Si/SiO_2 substrate was shown in Figure 37 (a). On the sample surface PMMA residues can be seen clearly even chemical cleaning procedure was applied. To observe the wrinkle formation, 15 nm thick SiO_2 thin film was deposited on CVD graphene at T_d = 90 ℃ by thermal evaporation system and cooled down the room temperature. After deposition SiO_2 thin film, optical microscopy measurements were taken (Figure 37 (b)) and hexagonal wrinkle structures were not observed on the CVD graphene. The reason of not observing wrinkle structures could be that graphene grown by CVD method is not homogeneous and defective. After the transfer procedure, graphene could be damaged

and defects may be occurred during the growth process. It can be concluded that the surface friction acting on SiO_2 thin film increased and thus strain was not sufficient to enough yield hexagonal wrinkles on the transferred graphene. Furthermore, another reason could be nanometer scale PMMA residues between graphene and SiO_2 thin film layer prevent the thermal strain between these two layers. However, for grown epitaxial graphene on SiC, there is no need to transfer onto another substrate and also it is chemically inert and clean when compared with CVD graphene.

4.7 Results and Discussions

In this chapter, the formation of hexagonal shaped SiO_2 wrinkles on monolayer epitaxial graphene was observed and characterized by optical microscopy, SEM and AFM. To understand the formation mechanism of wrinkle structures, 15 nm SiO_2 thin film was deposited both on as received SiC and on monolayer epitaxial graphene by thermal evaporation. It has been shown that the wrinkle network structure did not occur on bare SiC substrate unlike on epitaxial graphene layer. This was a result of negative thermal expansion coefficient of epitaxial graphene generated compressive strain on SiO_2 thin film unlike on bare SiC. Moreover, SiO_2 thin film has low adhesion on graphene layer than on SiC substrate hence, SiO_2 has a great tendency to form wrinkle structures.

After we observed the wrinkle structures on monolayer epitaxial graphene on SiC substrate, surface morphology and topography of these wrinkles were characterized by optical microscopy, SEM and AFM. By means of optical microscopy, the formation of hexagonal wrinkle structures was determined and the angle between the wrinkles was measured. In addition to these, wrinkles were categorized as a primary and secondary height protrusions depending on their propagation directions as observed by high resolution SEM measurements. The average height and the average width of these wrinkle structures were determined by AFM measurements. Two distinct characteristics of parallel strands were identified by AFM height profile measurements. The structural characteristics of the wrinkles were determined as hallow structures by means of HF etch experiments.

The propagation formation and dynamics of hexagonal wrinkles were observed with 50X magnification optical microscopy. In addition to this, spontaneous wrinkle networks propagation were measured with optical microscopy at 120 sec. time intervals.

The dynamics of these networks was identified as a result of sudden relaxation of SiO_2 thin film after cool down process due to the biaxial compressive strain.

To determine the effect of the compressive strain as a function of the temperature, 15 nm thick SiO_2 thin film was deposited with different deposition temperatures (T_d) on monolayer epitaxial graphene on SiC and this samples were cooled down to room temperature. The effect of the temperature differential (ΔT) on the wrinkle pattern was characterized by optical microscopy, SEM and AFM measurements. The average height and the width of the primary wrinkles was measured with different T_d. Nevertheless, the compressive strain acting on thin film was determined with respect to different ΔT and wrinkle spacing was measured experimentally. Theoretical results were compared with experimental data. Our experimental results manifested that temperature differential is directly related to the compressive strain and wrinkle spacing decreases as the strain increases.

CHAPTER 5

CONCLUSIONS

The aim of this thesis was to determine and characterize the surface morphology of self-assembled hexagonal shaped wrinkle structures of SiO_2 thin film on monolayer epitaxial graphene that was grown on SiC substrate due to the compressive strain. The thickness and homogeneity of epitaxial graphene were characterized by single point Raman spectroscopy and large area Raman mapping measurements. With different SiO_2 thin film deposition temperatures, the dynamics of wrinkle network was investigated. The dynamics and formation rate of the observed hexagonal structures was studied by Optical Microscopy. The observed network of wrinkles were found to comprise line shaped protrusions. The morphological and topographical characterizations were done by SEM and AFM measurements.

Prior to the SiO_2 thin film deposition process, large area graphene was grown at elevated temperatures above 1300 ℃ on SiC substrates under UHV conditions. To obtain monolayer epitaxial graphene, different growth parameters including temperature and time were applied. In order to determine the layer number of graphene, single point Raman spectroscopy measurements were carried out on the samples. The analysis, performed based on the Raman attenuation method suggest that graphene was grown as single layer on the SiC substrate. The thickness homogeneity of the grown epitaxial graphene samples was determined by large area Raman mapping. The optimum growth parameter to obtain monolayer epitaxial graphene was determined to be T = 1350 ℃ (growth temperature) and 3 min. (growth time).

Following the Raman spectroscopy analysis, 15 nm thick SiO_2 thin film was deposited thermally onto bare SiC and to monolayer epitaxial graphene that was produced on SiC substrate. Self-assembled hexagonal wrinkle network of SiO_2 was observed on epitaxial graphene rather than on bare SiC and the observed wrinkles were characterized by optical microscopy and SEM measurements. Wrinkle mesh density in a unit area and the magnitude of compressive strain due to temperature differential were determined by using the SEM measurement results. Primary and secondary ridge structures were observed and their characteristics were studied. The measurements revealed that primary

and secondary wrinkles intersect at an angle of about 118° ± 5 and the average mesh size of the wrinkles were determined as about 15 μm. The average height (0.38 μm) and width (2.4 μm) of the primary wrinkle structures were measured by AFM measurements. To understand the morphology of wrinkle structure in detail, the SiO_2 film and wrinkles were etched in HF solution. According to a set of HF etching experiments, we found that the wrinkle structures are hollow.

The dynamics of the wrinkle formation was investigated in real time by using optical microscopy right after the SiO_2 thin film deposition process. From these time dependent optical microscope measurements, the average velocity of wrinkle propagation was determined to be greater than 1 μm/s. This phenomena as explained in terms of the sudden relaxation of the SiO_2 thin film on epitaxial graphene layer due to the compressive strain. To investigate the effect of the strain as a function of temperature, SiO_2 thin film was deposited separately on a set of epitaxial graphene templates for three different deposition temperatures ranging between 60 ℃ and 150 ℃. The corresponding strain (σ) on SiO_2 thin film and wrinkle spacing (λ) was determined with respect to temperature differential (ΔT). While the strain increased on thin film due to increment of ΔT, the wrinkle to wrinkle spacing decreased and wrinkle density (ρ) increased correspondingly. Our experimentally obtained results are in good agreement with the calculated wrinkle spacing values.

Wrinkle formation were studied on monolayer CVD graphene after transferring it onto Si/SiO_2 substrate. The characterization were done by optical microscope measurements after depositing SiO_2 thin film on monolayer graphene. Contrary to epitaxial graphene, hexagonal wrinkle network was not observed on monolayer CVD grown graphene.

In this thesis, we concluded that the compressive thermal strain together with the adhesion and friction at the thin film/substrate interface play an important role on the formation of the observed wrinkle structures. The wrinkle spacing and corresponding mesh density of the SiO_2 wrinkle network were found to be strongly dependent on the magnitude of the thermal strain which changes as a function of the SiO_2 thin film deposition temperature. Our results demonstrate that epitaxial graphene, with its high chemical inertness and low surface friction, can serve as a suitable template to generate strain induced mechanical instabilities for thermally deposited thin films of amorphous or viscous materials like SiO_2. Our experimentally obtained results additionally imply

that epitaxial graphene with its high chemical inertness and low surface friction on SiC offers a great potential to be used as a conventional substrate in the realm of thin film metrology.

REFERENCES

(1) Seghir, R.; Arscott, S. Controlled Mud-Crack Patterning and Self-Organized Cracking of Polydimethylsiloxane Elastomer Surfaces. *Sci. Rep.* 2015, *5* (October), 14787.

(2) Xia, Y.; Kim, E.; Zhao, X.-M.; Rogers, J. a.; Prentiss, M.; Whitesides, G. M. Complex Optical Surfaces Formed by Replica Molding Against Elastomeric Masters. *Science*. 1996, pp 347–349.

(3) Khang, D. Y.; Rogers, J. A.; Lee, H. H. Mechanical Buckling: Mechanics, Metrology, and Stretchable Electronics. *Adv. Funct. Mater.* 2009, *19* (10), 1526–1536.

(4) Liu, Y.; Kenry; Guo, Y.; Sonam, S.; Hong, S. K.; Nai, M. H.; Nai, C. T.; Gao, L.; Chen, J.; Cho, B. J.; et al. Large-Area, Periodic, Hexagonal Wrinkles on Nanocrystalline Graphitic Film. *Adv. Funct. Mater.* 2015, *25* (34), 5492–5503.

(5) Petrović, M.; Sadowski, J. T.; Šiber, A.; Kralj, M. Wrinkles of Graphene on Ir(111): Macroscopic Network Ordering and Internal Multi-Lobed Structure. *Carbon N. Y.* 2015, *94* (111), 856–863.

(6) Yazyev, O. V; Louie, S. G. Electronic Transport in Polycrystalline Graphene. *Nat. Mater.* 2010, *9* (10), 806–809.

(7) Tapasztó, L.; Dumitrică, T.; Kim, S. J.; Nemes-Incze, P.; Hwang, C.; Biró, L. P. Breakdown of Continuum Mechanics for Nanometre-Wavelength Rippling of Graphene. *Nat. Phys.* 2012, *8* (October), 739–742.

(8) Srivastava, D.; Brenner, D. W.; Schall, J. D.; Ausman, K. D.; Yu, M. F.; Ruoff, R. S. Predictions of Enhanced Chemical Reactivity at Regions of Local Conformational Strain on Carbon Nanotubes: Kinky Chemistry. *J. Phys. Chem. B* 1999, *103* (21), 4330–4337.

(9) Deng, S.; Berry, V. Wrinkled, Rippled and Crumpled Graphene: An Overview of Formation Mechanism, Electronic Properties, and Applications. *Mater. Today* 2016, *19* (4), 197–212.

(10) Zang, J.; Ryu, S.; Pugno, N.; Wang, Q.; Tu, Q.; Buehler, M. J.; Zhao, X. Multifunctionality and Control of the Crumpling and Unfolding of Large-Area Graphene. *Nat. Mater.* 2013, *12* (4), 321–325.

(11) Chae, S. J.; Güneş, F.; Kim, K. K.; Kim, E. S.; Han, G. H.; Kim, S. M.; Shin, H.; Yoon, S. M.; Choi, J. Y.; Park, M. H.; et al. Synthesis of Large-Area Graphene Layers on Poly-Nickel Substrate by Chemical Vapor Deposition: Wrinkle Formation. *Adv. Mater.* 2009, *21* (22), 2328–2333.

(12) Spiecker, E.; Schmid, A. K.; Minor, A. M.; Dahmen, U.; Hollensteiner, S.; Jäger, W. Self-Assembled Nanofold Network Formation on Layered Crystal Surfaces during Metal Intercalation. *Phys. Rev. Lett.* 2006, *96* (8), 3–6.

(13) Zhu, W. J.; Low, T.; Perebeinos, V.; Bol, a a; Zhu, Y.; Yan, H. G.; Tersoff, J.; Avouris, P. Structure and Electronic Transport in Graphene Wrinkles. *Nano Lett.* 2012, *12*, 3431–3436.

(14) Liu, N.; Pan, Z.; Fu, L.; Zhang, C.; Dai, B.; Liu, Z. The Origin of Wrinkles on Transferred Graphene. *Nano Res.* 2011, *4* (10), 996–1004.

(15) Choi, Y. J.; Naoi, Y.; Tomita, T. Self-Organization of Highly Ordered Honeycomb Buckling Patterns in Crystalline Thin Films. *Jpn. J. Appl. Phys.* 2015, *54* (10).

(16) Park, H.-G.; Jeong, H.-C.; Jung, Y. H.; Seo, D.-S. Control of the Wrinkle Structure on Surface-Reformed Poly(dimethylsiloxane) via Ion-Beam Bombardment. *Sci. Rep.* 2015, *5* (January), 12356.

(17) Zhang, K.; Arroyo, M. Understanding and Strain-Engineering Wrinkle Networks in Supported Graphene through Simulations. *J. Mech. Phys. Solids* 2014, *72* (1), 61–74.

(18) Yoon, D.; Son, Y.-W.; Cheong, H. Negative Thermal Expansion Coefficient of Graphene Measured by Raman Spectroscopy. *Nano Lett.* 2011, *11* (8), 3227–3231.

(19) Bonaccorso, F.; Sun, Z.; Hasan, T.; Ferrari, A. C. Graphene Photonics and Optoelectronics. *Nat. Photonics* 2010, *4* (9), 611–622.

(20) Chung, C.; Kim, Y.-K.; Shin, D.; Ryoo, S.-R.; Hong, B. H.; Min, D.-H. Biomedical Applications of Graphene and Graphene Oxide. *Acc. Chem. Res.* 2013, *46* (10), 2211–2224.

(21) Moon, J. S.; Seo, H. C.; Stratan, F.; Antcliffe, M.; Schmitz, A.; Ross, R. S.; Kiselev, A. A.; Wheeler, V. D.; Nyakiti, L. O.; Gaskill, D. K.; et al. Lateral Graphene Heterostructure Field-Effect Transistor. *IEEE Electron Device Lett.* 2013, *34* (9), 1190–1192.

(22) Huang, Y.; Liang, J.; Chen, Y. An Overview of the Applications of Graphene-Based Materials in Supercapacitors. *Small* 2012, *8* (12), 1805–1834.

(23) Sun, X.; Liu, Z.; Welsher, K.; Robinson, J. T.; Goodwin, A.; Zaric, S.; Dai, H. Nano-Graphene Oxide for Cellular Imaging and Drug Delivery. *Nano Res* 2008, *1* (3), 203–212.

(24) Goehring, L. Evolving Fracture Patterns: Columnar Joints, Mud Cracks and Polygonal Terrain. *Philos. Trans. A. Math. Phys. Eng. Sci.* 2013, *371* (2004), 20120353.

(25) Neto, A. C.; Guinea, F.; Peres, N. M. Drawing Conclusions from Graphene. *Phys. World* 2006, *19* (11), 33–37.

(26) Wallace, P. R. The Band Theory of Graphite, *Phys. Rev.* 1947, *71*, 622.

(27) Novoselov, K. S.; Mccann, E.; Morozov, S. V; Fal'Ko, V. I.; Katsnelson, M. I.; Zeitler, U.; Jiang, D.; Schedin, F.; Geim, A. K. Unconventional Quantum Hall Effect and Berry's Phase of 2π in Bilayer Graphene. *Nat. Phys.* 2006, *2* (May 2013), 177.

(28) Novoselov, K. S.; Geim, A. K.; Morozov, S. V; Jiang, D.; Katsnelson, M. I.; Grigorieva, I. V; Dubonos, S. V; Firsov, A. A. Two-Dimensional Gas of Massless Dirac Fermions in Graphene. *Nature* 2005, *438* (7065), 197–200.

(29) Ghosh, S.; Calizo, I.; Teweldebrhan, D.; Pokatilov, E. P.; Nika, D. L.; Balandin, A. A.; Bao, W.; Miao, F.; Lau, C. N. Extremely High Thermal Conductivity of Graphene: Prospects for Thermal Management Applications in Nanoelectronic Circuits. *Appl. Phys. Lett.* 2008, *92* (15), 2008–2010.

(30) Mark, F.; Goerbig, O.; Notes, L. Introduction to the Physical Properties of Graphene. 2008.

(31) Vaziri, S. Fabrication and Characterization of Graphene Field Effect Transistors. *Thesis* 2011, 1–42.

(32) Georgantzinos, S. K.; Giannopoulos, G. I.; Anifantis, N. K. Numerical Investigation of Elastic Mechanical Properties of Graphene Structures. *Mater. Des.* 2010, *31* (10), 4646–4654.

(33) Lee, C.; Wei, X.; Kysar, J. W.; Hone, J.; =. Measurement of the Elastic Properties and Intrinsic Strength of Monolayer Graphene. *Science (80-.).* 2008, *321* (18 July 2008), 385–388.

(34) Liu, F.; Ming, P.; Li, J. Ab Initio Calculation of Ideal Strength and Phonon Instability of Graphene under Tension. *Phys. Rev. B - Condens. Matter Mater. Phys.* 2007, *76* (6), 1–7.

(35) Jing, Y.; Sun, Y.; Niu, H. Chirality and Size Dependent Elastic Properties of Silicene Nanoribbons under Uniaxial Tension. *Icf13* 2013, No. Md, 1–6.

(36) Castro Neto, A. H. .; Peres, N. M. R. .; Novoselov, K. S. .; Geim, A. K. .; Guinea, F. The Electronic Properties of Graphene. *Rev. Mod. Phys.* 2009, *81* (1), 109–162.

(37) Lin, I. Optical Properties of Graphene from the THz to the Visible Spectral Region. *Thesis* 2012, Date of access:12/04/2016.

(38) Reich, S.; Maultzsch, J.; Thomsen, C.; Ordejón, P. Tight-Binding Description of Graphene. *Phys. Rev. B* 2002, *66* (3), 1–5.

(39) Eda, G.; Fanchini, G.; Chhowalla, M. Large-Area Ultrathin Films of Reduced Graphene Oxide as a Transparent and Flexible Electronic Material. *Nat. Nanotechnol.* 2008, *3* (5), 270–274.

(40) Wang, Y.; Li, Z.; Wang, J.; Li, J.; Lin, Y. Graphene and Graphene Oxide: Biofunctionalization and Applications in Biotechnology. *Trends Biotechnol*. 2011, *29* (5), 205–212.

(41) Kusdemir, E.; Özkendir, D.; Fırat, V.; Çelebi, C. Epitaxial Graphene Contact Electrode for Silicon Carbide Based Ultraviolet Photodetector. *J. Phys. D. Appl. Phys. 95104*, 95104.

(42) Liu, Z.; Li, J.; Sun, Z.-H.; Tai, G.; Lau, S.-P.; Yan, F. The Application of Highly Doped Single-Layer Graphene as the Top Electrodes of Semitransparent Organic Solar Cells. *ACS Nano* 2012, *6* (1), 810–818.

(43) Miao, X.; Tongay, S.; Petterson, M. K.; Berke, K.; Rinzler, A. G.; Appleton, B. R.; Hebard, A. F. High E Ffi Ciency Graphene Solar Cells by Chemical Doping. *Nano Lett.* 2012, *12*, 6–11.

(44) Nair, R. R.; Grigorenko, A. N.; Blake, P.; Novoselov, K. S.; Booth, T. J.; Peres, N. M. R.; Stauber, T.; Geim, A. K. Fine Structure Constant Defines Visual Transparency of Graphene. *Science (80-.).* 2008, *320* (5881), 1308.

(45) Novoselov, K. S. Nobel Lecture: Graphene: Materials in the Flatland. *Rev. Mod. Phys.* 2011, *83* (3), 837–849.

(46) Falkovsky, L. a. Optical Properties of Graphene. *IOP Sci.* 2008, *12004*, 5.

(47) Lee, C. J.; Cha, H. G.; Hong, S. K.; Doh, S. H.; Koo, Y. S.; Cho, B. J.; Hahm, S. H. GaN MSM UV Sensor Using Multi-Layer Graphene Schottky Electrodes. *Appl. Mech. Mater.* 2014, *481*, 146–149.

(48) Yi, M.; Shen, Z. A Review on Mechanical Exfoliation for the Scalable Production of Graphene. *J. Mater. Chem. A* 2015, *3* (22), 11700–11715.

(49) Bolotin, K. I.; Sikes, K. J.; Jiang, Z.; Klima, M.; Fudenberg, G.; Hone, J.; Kim, P.; Stormer, H. L. Ultrahigh Electron Mobility in Suspended Graphene. *Solid State Commun.* 2008, *146* (9–10), 351–355.

(50) Vasudevan, A. V.; Zhang, K.; Arroyo, M. Curved Folds on Supported Graphene Under. 2014, No. Wccm Xi, 11–12.

(51) Naseem, H. CVD Graphene Growth Mechanism on Nickel Thin Films. 2014, *446* (7131), 7131.

(52) Mattevi, C.; Kim, H.; Chhowalla, M.; Neto, A. H. C.; Guinea, F.; Peres, N. M. R.; Novoselov, K. S.; Geim, A. K.; Chen, J.-H.; Jang, C.; et al. A Review of Chemical Vapour Deposition of Graphene on Copper. *J. Mater. Chem.* 2011, *21* (10), 3324–3334.

(53) Obraztsov, A. N.; Obraztsova, E. A.; Tyurnina, A. V.; Zolotukhin, A. A. Chemical Vapor Deposition of Thin Graphite Films of Nanometer Thickness. *Carbon N. Y.* 2007, *45* (10), 2017–2021.

(54) Fuente, J. D. La; Santiago, J.; Román, A.; Dumitrache, C.; Casasanto, D. Production, Propereties and Potential of Graphene. *Psychol. Sci.* 2014, *25* (9), 1682–1690.

(55) Li, X.; Cai, W.; An, J.; Kim, S.; Nah, J.; Yang, D.; Piner, R.; Velamakanni, A.; Jung, I.; Tutuc, E.; et al. Large-Area Synthesis of High-Quality and Uniform Graphene Films on Copper Foils. *Science (80-.).* 2009, *324* (5932), 1312–1314.

(56) Gomez De Arco L, Zhang Y, Schlenker CW, Ryu K, Thompson ME, Z. C. Continuous, Highly Flexible, and Transparent Graphene Films by Chemical Vapor Deposition for Organic Photovoltaics. *ACS Nano* 2010, *4* (5), 2865–2873.

(57) Tianyi He, K. Characterization of Graphene-Substrate Interactions Using STM. 2013.

(58) Kim, K.; Lee, Z.; Regan, W.; Kisielowski, C.; Crommie, M. F.; Zettl, A. Grain Boundary Mapping in Polycrystalline Graphene. *ACS Nano* 2011, *5* (3), 2142–2146.

(59) Demirbas T, B. M. Z. Nanoscale Tribology of Graphene Grown by Chemical Vapor Deposition and Transferred onto Silicon Oxide Substrates. *J. Mater. Res.* 2016, *31* (13), 1914–1923.

(60) de Heer, W. A.; Berger, C.; Wu, X.; First, P. N.; Conrad, E. H.; Li, X.; Li, T.; Sprinkle, M.; Hass, J.; Sadowski, M. L.; et al. Epitaxial Graphene. *Solid State Commun.* 2007, *143* (1–2), 92–100.

(61) Riedl, C.; Coletti, C.; Starke, U. Structural and Electronic Properties of Epitaxial Graphene on SiC(0001): A Review of Growth, Characterization, Transfer Doping and Hydrogen Intercalation. *J. Phys. D. Appl. Phys.* 2010, *43* (37), 374009.

(62) Berger, C.; Song, Z.; Li, T.; Li, X.; Ogbazghi, A. Y.; Feng, R.; Dai, Z.; Marchenkov, A. N.; Conrad, E. H.; First, P. N.; et al. Ultrathin Epitaxial Graphite: 2D Electron Gas Properties and a Route toward Graphene-Based Nanoelectronics. *J. Phys. Chem. B* 2004, *108* (52), 19912–19916.

(63) Sadowski, M. L.; Martinez, G.; Potemski, M.; Berger, C.; De Heer, W. A. Landau Level Spectroscopy of Ultrathin Graphite Layers. *Phys. Rev. Lett.* 2006, *97* (26), 1–4.

(64) Hass, J.; Feng, R.; Li, T.; Li, X.; Zong, Z.; De Heer, W. A.; First, P. N.; Conrad, E. H.; Jeffrey, C. A.; Berger, C. Highly Ordered Graphene for Two Dimensional Electronics. *Appl. Phys. Lett.* 2006, *89* (14), 8–10.

(65) Articlepress. Synthesis and Characterization of Atomically Thin Graphite Lms on a Silicon Carbide Substrate. *J. Phys. Chem. Solids* 2006, *67*, 2172–2177.

(66) Senturia, S. D. *Microsystem Design*; Springer, 2000.

(67) Levy, J. S.; Marchant, D. R.; Head, J. W. Thermal Contraction Crack Polygons on Mars: A Synthesis from HiRISE, Phoenix, and Terrestrial Analog Studies. *Icarus* 2010, *206* (1), 229–252.

(68) Martin, J.; Akerman, N.; Ulbricht, G.; Lohmann, T.; Smet, J. H.; von Klitzing, K.; Yacoby, A. Observation of Electron-Hole Puddles in Graphene Using a Scanning Single Electron Transistor. *Nat. Phys.* 2007, *4* (February), 13.

(69) Partovi-Azar, P.; Nafari, N.; Tabar, M. R. R. Interplay between Geometrical Structure and Electronic Properties in Rippled Free-Standing Graphene. *Phys. Rev. B - Condens. Matter Mater. Phys.* 2011, *83* (16), 1–5.

(70) Levy, N.; Burke, S. A.; Meaker, K. L.; Panlasigui, M.; Zettl, A.; Guinea, F.; Castro Neto, A. H.; Crommie, M. F. Strain-Induced Pseudo-Magnetic Fields Greater than 300 T in Graphene Nanobubbles. *Science (80-.).* 2010, *544* (July), 544–547.

(71) Rodríguez-Hernández, J. Wrinkled Interfaces: Taking Advantage of Surface Instabilities to Pattern Polymer Surfaces. *Prog. Polym. Sci.* 2015, *42*, 1–41.

(72) Xia, Z. C.; Hutchinson, J. W. Crack Patterns in Thin Films. *J. Mech. Phys. Solids* 2000, *48* (6), 1107–1131.

(73) Jiang, T.; Huang, R.; Zhu, Y. Interfacial Sliding and Buckling of Monolayer Graphene on a Stretchable Substrate. *Adv. Funct. Mater.* 2014, *24* (3), 396–402.

(74) Filleter, T.; McChesney, J. L.; Bostwick, A.; Rotenberg, E.; Emtsev, K. V.; Seyller, T.; Horn, K.; Bennewitz, R. Friction and Dissipation in Epitaxial Graphene Films. *Phys. Rev. Lett.* 2009, *102* (8), 1–4.

(75) Zhang, D.; Jin, Z.; Shi, J.; Ma, P.; Peng, S.; Liu, X.; Ye, T. The Anistropy of Field Effect Mobility of CVD Graphene Grown on Copper Foil. *Small* 2014, *10* (9), 1761–1764.

(76) Zhang, K.; Arroyo, M. Understanding and Strain-Engineering Wrinkle Networks in Supported Graphene through Simulations. *J. Mech. Phys. Solids* 2014, *72* (1), 61–74.

(77) Prakash, G.; Bolen, M. L.; Colby, R.; Stach, E. A.; Capano, M. A.; Reifenberger, R. Nanomanipulation of Ridges in Few-Layer Epitaxial Graphene Grown on the Carbon Face of 4H-SiC. *New J. Phys.* 2010, *12*.

(78) Borysiuk, J.; Bozek, R.; Grodecki, K.; Wysmołek, A.; Strupiński, W.; Stępniewski, R.; Baranowski, J. M. Transmission Electron Microscopy Investigations of Epitaxial Graphene on C-Terminated 4H-SiC. *J. Appl. Phys.* 2010, *108* (1).

(79) Xu, K.; Cao, P.; Heath, J. R. Scanning Tunneling Microscopy Characterization of the Electrical Properties of Wrinkles in Exfoliated Graphene Monolayers. *Nano Lett.* 2009, *9* (12), 4446–4451.

(80) Spetz, A.; Unéus, L. SiC Based Field Effect Gas Sensors for Industrial Applications. *Phys. Stat. Sol.* 2001, *25* (1), 15–25.

(81) Li, X. Epitaxial Graphene Films on SiC: Growth, Characterization, and Devices. 2008, August.

(82) Casady, J. B.; Johnson, R. W. Status of Silicon Carbide (SiC) as a Wide-Bandgap Semiconductor for High-Temperature Applications: A Review. *Solid. State. Electron.* 1996, *39* (96), 1409–1422.

(83) Li, Z.; Bradt, R. C. Thermal Expansion and Thermal Expansion Anisotropy of SiC Polytypes. *J. Am. Ceram. Soc.* 1987, *70* (7), 445–448.

(84) Wu, R.; Zhou, K.; Yue, C. Y.; Wei, J.; Pan, Y. Recent Progress in Synthesis, Properties and Potential Applications of SiC Nanomaterials. *Prog. Mater. Sci.* 2015, *72*, 1–60.

(85) Rao, M. V. Maturing Ion-Implantation Technology and Its Device Applications in SiC. *2001 Int. Semicond. Device Res. Symp. ISDRS 2001 - Proc.* 2001, *47*, 519–522.

(86) Dimitrakopoulos, C.; Lin, Y.-M.; Grill, A.; Farmer, D. B.; Freitag, M.; Sun, Y.; Han, S.-J.; Chen, Z.; Jenkins, K. a.; Zhu, Y.; et al. Wafer-Scale Epitaxial Graphene Growth on the Si-Face of Hexagonal SiC (0001) for High Frequency Transistors. *J. Vac. Sci. Technol. B* 2010, *106* (1), 30.

(87) Han, Y.; Aoyama, T.; Ichimiya, A.; Hisada, Y.; Mukainakano, S. Atomic Models of (√3×√3)R30° Reconstruction on Hexagonal 6H–SiC(0001) Surface. *J. Vac. Sci. Technol. B Microelectron. Nanom. Struct.* 2001, *19* (5), 1972.

(88) Emtsev, K. V.; Speck, F.; Seyller, T.; Ley, L.; Riley, J. D. Interaction, Growth, and Ordering of Epitaxial Graphene on SiC{0001} Surfaces: A Comparative Photoelectron Spectroscopy Study. *Phys. Rev. B - Condens. Matter Mater. Phys.* 2008, *77* (15), 1–10.

(89) Abderrazak, H.; Selmane, E.; Hadj, B. Silicon Carbide : Synthesis and Properties. *Prop. Appl. Silicon Carbide* 2011, No. C, 361–389.

(90) Boehm, H. P.; Setton, R.; Stumpp, E. Nomenclature and Terminology of Graphite Intercalation Compounds (IUPAC Recommendations 1994). *Pure Appl. Chem.* 1994, *66* (9), 1893–1901.

(91) Van Bommel, A. J.; Crombeen, J. E.; Van Tooren, A. LEED and Auger Electron Observations of the SiC(0001) Surface. *Surf. Sci.* 1975, *48* (2), 463–472.

(92) Ibrahim, A. The Growth of Epitaxial Graphene for Two-Dimensional Electronics A Thesis Submitted to. 2015, July.

(93) Forbeaux, I.; Themlin, J.-M.; Debever, J.-M. Heteroepitaxial Graphite on 6H-SiC(0001): Interface Formation through Conduction-Band Electronic Structure. *Phys. Rev. B* 1998, *58* (24), 16396–16406.

(94) Van Elsbergen, V.; Kampen, T. U.; Mönch, W. Surface Analysis of 6H-SiC. *Surf. Sci.* 1996, *365* (2), 443–452.

(95) Rutter, G. M.; Guisinger, N. P.; Crain, J. N.; Jarvis, E. A. A.; Stiles, M. D.; Li, T.; First, P. N.; Stroscio, J. A. Imaging the Interface of Epitaxial Graphene with Silicon Carbide via Scanning Tunneling Microscopy. *Phys. Rev. B - Condens. Matter Mater. Phys.* 2007, *76* (23), 1–6.

(96) Riedl, C.; Starke, U.; Bernhardt, J.; Franke, M.; Heinz, K. Structural Properties of the Graphene-SiC(0001) Interface as a Key for the Preparation of Homogeneous Large-Terrace Graphene Surfaces. *Phys. Rev. B - Condens. Matter Mater. Phys.* 2007, *76* (24), 1–8.

(97) Hass, J.; de Heer, W. a; Conrad, E. H. The Growth and Morphology of Epitaxial Multilayer Graphene. *J. Phys. Condens. Matter* 2008, *20* (32), 323202.

(98) de Heer, W. a.; Berger, C.; Ruan, M.; Sprinkle, M.; Li, X.; Hu, Y.; Zhang, B.; Hankinson, J.; Conrad, E. H. Large Area and Structured Epitaxial Graphene Produced by Confinement Controlled Sublimation of Silicon Carbide. *Pnas* 2011, *108* (41), 16900–16905.

(99) Jernigan, G. G.; VanMil, B. L.; Tedesco, J. L.; Tischler, J. G.; Glaser, E. R.; Davidson, A.; Campbell, P. M.; Gaskill, D. K. Comparison of Epitaxial Graphene on Si-Face and C-Face 4H SiC Formed by Ultrahigh Vacuum and RF Furnace Production. *Nano Lett.* 2009, *9* (7), 2605–2609.

(100) Norimatsu, W.; Kusunoki, M. Epitaxial Graphene on SiC{0001}: Advances and Perspectives. *Phys. Chem. Chem. Phys.* 2014, *16*, 3501–3511.

(101) Çelebi, C.; Yanik, C.; Demirkol, A. G.; Kaya, I. I. The Effect of a SiC Cap on the Growth of Epitaxial Graphene on SiC in Ultra High Vacuum. *Carbon N. Y.* 2012, *50* (8), 3026–3031.

(102) Çelebi, C. Control of the Graphene Growth Rate on Capped SiC Surface under Strong Si Confinement. 2013, *264*, 56–60.

(103) Raman, C. V., K. K. S. A New Class of Spectra due to Secundary Radiation. *Indian J. Phys.* 1928, *2*, 399–419.

(104) Ferrari, A. C.; Meyer, J. C.; Scardaci, V.; Casiraghi, C.; Lazzeri, M.; Mauri, F.; Piscanec, S.; Jiang, D.; Novoselov, K. S.; Roth, S.; et al. Raman Spectrum of Graphene and Graphene Layers. *Phys. Rev. Lett.* 2006, *97* (18).

(105) You, Y.; Ni, Z.; Yu, T.; Shen, Z.; You, Y.; Ni, Z.; Yu, T.; Shen, Z. Edge Chirality Determination of Graphene by Raman Spectroscopy Edge Chirality Determination of Graphene by Raman Spectroscopy. 2008, *163112*, 1–4.

(106) Hao, Y.; Wang, Y.; Wang, L.; Ni, Z.; Wang, Z.; Wang, R.; Koo, C. K.; Shen, Z.; Thong, J. T. L. Probing Layer Number and Stacking Order of Few-Layer Graphene by Raman Spectroscopy . 2010, 195–200.

(107) Ezawa, M. Peculiar Width Dependence of the Electronic Properties of Carbon Nanoribbons. 2006, No. September 2005, 1–8.

(108) Ferrari, A. C. Raman Spectroscopy of Graphene and Graphite : Disorder , Electron – Phonon Coupling , Doping and Nonadiabatic Effects. 2007, *143*, 47–57.

(109) Ni, Z. H.; Chen, W.; Fan, X. F.; Kuo, J. L.; Yu, T.; Wee, A. T. S.; Shen, Z. X. Raman Spectroscopy of Epitaxial Graphene on a SiC Substrate. *Phys. Rev. B - Condens. Matter Mater. Phys.* 2008, *77* (11), 1–6.

(110) Duhee, Y.; Hyerim, M.; Hyeonsik, C.; JinSik, C.; JungAe, C.; BaeHo, P. Variations in the Raman Spectrum as a Function of the Number of Graphene Layers. *J. Korean Phys. Soc.* 2009, *55* (32), 1299.

(111) Shivaraman, S.; Chandrashekhar, M. V. S.; Boeckl, J. J.; Spencer, M. G. Thickness Estimation of Epitaxial Graphene on SiC Using Attenuation of Substrate Raman Intensity.

(112) Binnig, G.; Quate, C.; Gerber, C. Atomic Force Microscope. *Physical Review Letters*. 1986, pp 930–933.

(113) Jalili, N.; Laxminarayana, K. A Review of Atomic Force Microscopy Imaging Systems : Application to Molecular Metrology and Biological Sciences. 2004, *14*, 907–945.

(114) Butt, H. J. Measuring Electrostatic, van Der Waals, and Hydration Forces in Electrolyte Solutions with an Atomic Force Microscope. *Biophys. J.* 1991, *60* (December), 1438–1444.

(115) Sameshima, T.; Kohno, A.; Sekiya, M.; Hara, M.; Sano, N. SiO2 Formation by Thermal Evaporation of SiO in Oxygen Atmosphere Used to Fabrication of High Performance Polycrystalline Silicon Thin Film Transistors. *Appl. Phys. Lett.* 1994, *64* (8), 1018–1020.

(116) Tada, H.; Kumpel, A. E.; Lathrop, R. E.; Slanina, J. B.; Nieva, P.; Zavracky, P.; Miaoulis, I. N.; Wong, P. Y. Thermal Expansion Coefficient of Polycrystalline Silicon and Silicon Dioxide Thin Films at High Temperatures. *J. Appl. Phys.* 2000, *87* (9), 4189–4193.

(117) Cotterell, B.; Chen, Z. Buckling and Cracking of Thin Films on Compliant Substrates under Compression. 2000, 169–179.

(118) Budrikis, Z.; Sellerio, A. L.; Bertalan, Z.; Zapperi, S. Wrinkle Motifs in Thin Films. 2015, 1–7.

(119) Luxmi; Srivastava, N.; Freenstra, R. M. Formation of Epitaxial Graphene on SiC(0001) Using Vacuum or Argon Environment. *J. Chem. Inf. Model.* 2013, *53* (9), 1689–1699.

(120) Hu, Y.; Ruan, M.; Guo, Z.; Dong, R.; Palmer, J.; Hankinson, J.; Berger, C.; de Heer, W. A. Structured Epitaxial Graphene: Growth and Properties. *J. Chem. Inf. Model.* 2013, *53* (9), 1689–1699.

(121) Zhao, Y.; Cao, Y.; Hong, W.; Khurram, M.; Feng, X. Towards a Quantitative Understanding of Period-Doubling Wrinkling Patterns Occurring in Film / Substrate Bilayer Systems Subject Areas : 2015.

(122) Huang, R.; Suo, Z. Wrinkling of a Compressed Elastic Film on a Viscous Layer. 2012, *1135* (2002), 1791–1802.

(123) Zhao, J.-H.; Ryan, T.; Ho, P. S.; McKerrow, A. J.; Shih, W.-Y. Measurement of Elastic Modulus, Poisson Ratio, and Coefficient of Thermal Expansion of on-Wafer Submicron Films. *J. Appl. Phys.* 1999, *85* (1999), 6421–6424.

(124) Kobeda, E. SiO2 Film Stress Distribution during Thermal Oxidation of Si. *J. Vac. Sci. Technol. B Microelectron. Nanom. Struct.* 1988, *6* (2), 574.